U.S. Department of Transportation

Federal Railroad Administration

Monitoring Longitudinal Rail Stress Using Diffuse Ultrasonic Backscatter

Office of Research,
Development
and Technology
Washington, DC 20590

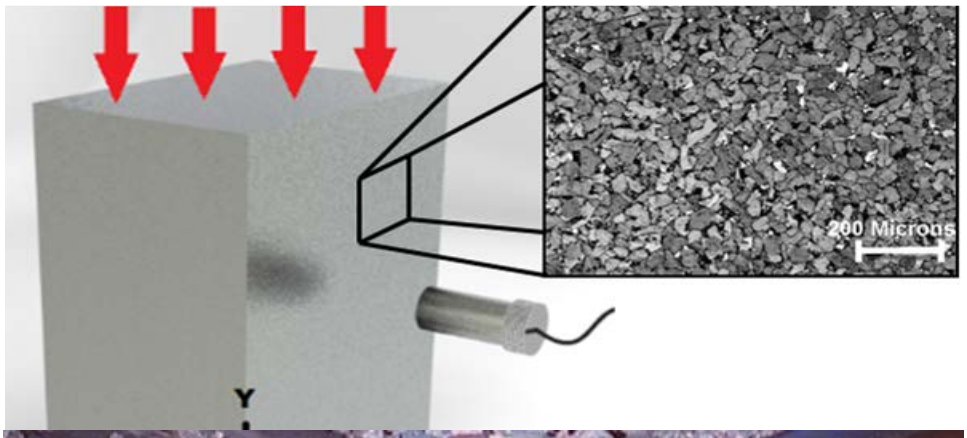

DOT/FRA/ORD-17/15

Final Report
September 2017

REPORT DOCUMENTATION PAGE

Form Approved
OMB No. 0704-0188

1. AGENCY USE ONLY (Leave blank)	2. REPORT DATE	3. REPORT TYPE AND DATES COVERED
	September 2017	Technical Report

4. TITLE AND SUBTITLE
Monitoring Longitudinal Rail Stress Using Diffuse Ultrasonic Backscatter

5. FUNDING NUMBERS
FR-RRD-0011-10-01-00

6. AUTHOR(S)
Joseph A. Turner, PhD

7. PERFORMING ORGANIZATION NAME(S) AND ADDRESS(ES)
University of Nebraska-Lincoln
1400 R Street
Lincoln, NE 68588

8. PERFORMING ORGANIZATION REPORT NUMBER

9. SPONSORING/MONITORING AGENCY NAME(S) AND ADDRESS(ES)
U.S. Department of Transportation
Federal Railroad Administration
Office of Railroad Policy and Development
Office of Research, Development and Technology
Washington, DC 20590

10. SPONSORING/MONITORING AGENCY REPORT NUMBER
DOT/FRA/ORD-17/15

11. SUPPLEMENTARY NOTES
COR: Mahmood Fateh

12a. DISTRIBUTION/AVAILABILITY STATEMENT
This document is available to the public through the FRA Web site at http://www.fra.dot.gov.

12b. DISTRIBUTION CODE

13. ABSTRACT (Maximum 200 words)

In this report, research was conducted at the University of Nebraska-Lincoln pertaining to the use of ultrasound scattering from polycrystalline grains to estimate and monitor stress in rail. The report presents a comprehensive discussion of the theoretical model of the scattering process, including all measurement parameters, such as the properties of the ultrasonic transducers. The results showed that the grain scattering was sensitive to changes in applied mechanical or thermal stresses, and that each transducer configuration had a different sensitivity to the changes in stress, as expected. This grain scattering approach could be used to quantify the microstructure of rail in the field as a function of position. However, experimental variations could not be reduced to the point of stress estimates being made reliably by using the approaches examined here.

14. SUBJECT TERMS
stress in rail; ultrasonic transducers; ultrasound scattering; theoretical model of the scattering process; prototype devices for stress estimations in rail; laboratory and field tests

15. NUMBER OF PAGES
73

16. PRICE CODE

17. SECURITY CLASSIFICATION OF REPORT	18. SECURITY CLASSIFICATION OF THIS PAGE	19. SECURITY CLASSIFICATION OF ABSTRACT	20. LIMITATION OF ABSTRACT
Unclassified	Unclassified	Unclassified	

METRIC/ENGLISH CONVERSION FACTORS

ENGLISH TO METRIC

LENGTH (APPROXIMATE)

1 inch (in)	=	2.5 centimeters (cm)
1 foot (ft)	=	30 centimeters (cm)
1 yard (yd)	=	0.9 meter (m)
1 mile (mi)	=	1.6 kilometers (km)

AREA (APPROXIMATE)

1 square inch (sq in, in^2)	=	6.5 square centimeters (cm^2)
1 square foot (sq ft, ft^2)	=	0.09 square meter (m^2)
1 square yard (sq yd, yd^2)	=	0.8 square meter (m^2)
1 square mile (sq mi, mi^2)	=	2.6 square kilometers (km^2)
1 acre = 0.4 hectare (he)	=	4,000 square meters (m^2)

MASS - WEIGHT (APPROXIMATE)

1 ounce (oz)	=	28 grams (gm)
1 pound (lb)	=	0.45 kilogram (kg)
1 short ton = 2,000 pounds (lb)	=	0.9 tonne (t)

VOLUME (APPROXIMATE)

1 teaspoon (tsp)	=	5 milliliters (ml)
1 tablespoon (tbsp)	=	15 milliliters (ml)
1 fluid ounce (fl oz)	=	30 milliliters (ml)
1 cup (c)	=	0.24 liter (l)
1 pint (pt)	=	0.47 liter (l)
1 quart (qt)	=	0.96 liter (l)
1 gallon (gal)	=	3.8 liters (l)
1 cubic foot (cu ft, ft^3)	=	0.03 cubic meter (m^3)
1 cubic yard (cu yd, yd^3)	=	0.76 cubic meter (m^3)

TEMPERATURE (EXACT)

[(x-32)(5/9)] °F = y °C

METRIC TO ENGLISH

LENGTH (APPROXIMATE)

1 millimeter (mm)	=	0.04 inch (in)
1 centimeter (cm)	=	0.4 inch (in)
1 meter (m)	=	3.3 feet (ft)
1 meter (m)	=	1.1 yards (yd)
1 kilometer (km)	=	0.6 mile (mi)

AREA (APPROXIMATE)

1 square centimeter (cm^2)	=	0.16 square inch (sq in, in^2)
1 square meter (m^2)	=	1.2 square yards (sq yd, yd^2)
1 square kilometer (km^2)	=	0.4 square mile (sq mi, mi^2)
10,000 square meters (m^2)	=	1 hectare (ha) = 2.5 acres

MASS - WEIGHT (APPROXIMATE)

1 gram (gm)	=	0.036 ounce (oz)
1 kilogram (kg)	=	2.2 pounds (lb)
1 tonne (t)	=	1,000 kilograms (kg)
	=	1.1 short tons

VOLUME (APPROXIMATE)

1 milliliter (ml)	=	0.03 fluid ounce (fl oz)
1 liter (l)	=	2.1 pints (pt)
1 liter (l)	=	1.06 quarts (qt)
1 liter (l)	=	0.26 gallon (gal)
1 cubic meter (m^3)	=	36 cubic feet (cu ft, ft^3)
1 cubic meter (m^3)	=	1.3 cubic yards (cu yd, yd^3)

TEMPERATURE (EXACT)

[(9/5) y + 32] °C = x °F

QUICK INCH - CENTIMETER LENGTH CONVERSION

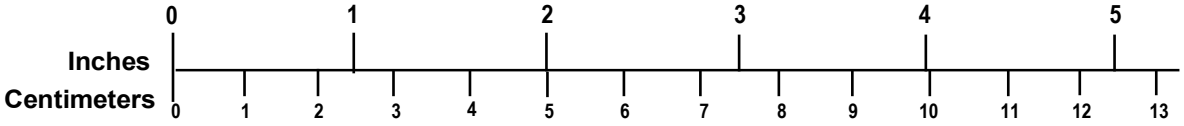

QUICK FAHRENHEIT - CELSIUS TEMPERATURE CONVERSIO

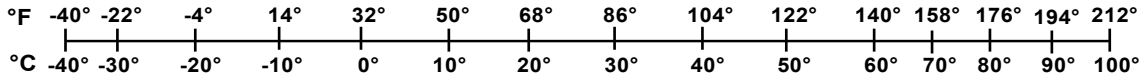

For more exact and or other conversion factors, see NIST Miscellaneous Publication 286, Units of Weights and Measures. Price $2.50 SD Catalog No. C13 10286

Updated 6/17/98

Contents

Figures

Tables

Executive Summary

In this report, research sponsored by the Federal Railroad Administration (FRA) was conducted and completed in May 2013 by the University of Nebraska-Lincoln, pertaining to the use of ultrasound scattering from polycrystalline grains to estimate and monitor stress in rail. The report presents a comprehensive discussion of the theoretical model of the scattering process, including all measurement parameters, such as the properties of the ultrasonic transducers.

Experiments were used to show that the model could predict the grain scattering for a given grain size in stress-free polycrystalline samples for different transducer configurations that include one transducer (pulse-echo) or two transducers (pitch-catch). The connection between the scattering and an applied stress in the material was then derived and used to show that different measurement configurations could have different sensitivities to the applied stress. This information was used to design several prototype devices for stress estimations in rail, which were tested in the laboratory and in field conditions.

The results showed that the grain scattering was sensitive to changes in applied mechanical or thermal stresses, and that each transducer configuration had a different sensitivity to the changes in stress, as expected. This grain scattering approach could be used to quantify the microstructure of rail in the field as a function of position. However, experimental variations could not be reduced to the point of stress estimates being made reliably by using the approaches examined here.

1. Introduction

Over the past several decades, railroads have continued to expand their use of continuously welded rail (CWR) as part of their major freight and passenger transportation lines. CWR brings together nominal quarter-mile lengths of rail into sections reaching as far as 6 miles (Szelazek, 1992). The transition from jointed rail to CWR could be attributed to recently improved thermite and electric welding techniques, along with many cost-saving factors. This transition resulted in increased efficiency in rail installation and a large decrease in track maintenance costs required over the service life of rail (Szelazek, 1998).

Previous rail installations utilized expansion joints and fish plates to connect sections of rail. The elimination of those joints greatly reduces the dynamic loads that result from the interaction of the wheels of heavy freight trains with the rail. The reduced loads result in decreased deterioration and wear of both the rail and the train wheels, allowing higher transit speeds with an increase in track longevity. All these factors contribute to millions of dollars in cost savings and have played a role in the reemergence of the railroad industry in the second half of the 20th century. In 2007, the number of installed CWR track mileage used in Class 1 railroads reached 96,500 miles (American Association of Railroads, 2013).

Although CWR has had a positive impact on the railroads, it has also created an additional safety concern associated with track buckling. Without the ability of the rail to expand freely along its length, it is forced to expand laterally when compressive stresses exceed the buckling threshold. The lateral movement is restricted through the use of sleepers and anchors designed to prevent extreme lateral movement or buckling; however, the design stresses can be difficult to predict. In addition, during the service life of rail, the stress distribution can change with variable train loads and environmental conditions. Thus, the ability to monitor and maintain stress in the rail has been a major research thrust aimed at preventing catastrophic buckling events.

1.1 Background

Structural health monitoring through stress field measurements is a necessity throughout many different areas in industry. Stress field measurement techniques extend to applications involving railroad wheels and tracks, civil structures such as dams and bridges, and other applications that require continual stress monitoring for integral usage. In many instances, the current methods (such as strain gauges) provide information at only a single location. In addition, the permanent placement of strain gauges proves to be laborious and costly in dealing with calibration and general maintenance. X-ray and neutron diffraction techniques are also able to monitor localized changes in strain. These represent nondestructive methods to measure stress fields, but often are impractical due to high costs and constraints on portability. Other nondestructive methods, such as ultrasonic techniques, have been developed and used to supplant the inadequacies of strain gauges and offer portable systems at lower costs compared to diffraction techniques. This report discusses the utility of ultrasonic scattering for stress measurement.

Ultrasonic techniques based on the theory of acoustoelasticity have been used in the past to relate applied stresses to changes in the velocity of elastic waves. Bergman and Shahbender (1958) were among the first researchers who showed changes in shear and longitudinal wave speed as a function of load in samples of aluminum columns. Egle and Bray (1976) studied waves propagating in directions parallel and perpendicular to the loading direction in samples of rail steel. They found relative changes in wave speed on the order of 10^{-3} as a function of strain for

samples loaded up to 26.7 kilonewtons (kN). The practical applicability of such methods (involving a pitch-catch configuration) is limited. Generally, the separation distance between source and receiver must be large enough to allow for sufficient resolution of the received signals. Also, the surface geometry needs to be uniform to prevent edge reflection effects. These factors place constraints on the shape and dimensions of a measurable sample. Recently, researchers have applied diffuse ultrasonic techniques to determine stress fields in a variety of materials. For example, Larose and Hall (2009) were able to show the linear dependence between wave speed and uniaxial stress variations in samples of aggregate concrete.

Ultrasonic scattering techniques based on diffuse backscatter can be used to garner information about the microstructure of a material, because they exploit the scattering of ultrasonic waves from the heterogeneous composition. They are often used to determine the presence of cracks, voids, and inclusions, and to characterize microstructure. For a pulse-echo configuration, the statistical analysis usually is developed from the spatial statistics of the acquired signals (Margetan et al., 1991; Ghoshal et al., 2007; Ghoshal and Turner, 2010). Recently, a statistical model was used to quantify the spatial variance of such signals, thus allowing quantitative measurements to be made (Ghoshal et al., 2007; Ghoshal and Turner, 2010). Because the applied stress affects the material at the grain level, the scattered ultrasonic field is also expected to change with stress. A model that predicts the change in scattering due to an applied stress was subsequently developed by Turner and Ghoshal (2010). The relationship between stress and ultrasonic scattering forms the basis for this project.

1.2 Objectives

The primary objective of this research project was to develop a stress monitoring method based on diffuse ultrasonic backscatter (DUB). In order for this objective to be achieved the following tasks were identified:

- Develop comprehensive theoretical models of the diffuse ultrasonic backscatter for pulse-echo and pitch-catch transducer configurations, and confirm the models with experimental measurements.
- Develop experimental devices that can be used to measure diffuse ultrasonic signals on railroad rail, both for use in the lab and for field measurements.
- Develop appropriate signal processing schemes to analyze measured signals and interpret the signals with respect to the applied stresses.
- Develop a test site with several stress modules that can be used as a test bed for the measurements.
- Test the ability of the devices developed to monitor stress in rail, using field tests at test sites with stress modules for comparison.

1.3 Overall Approach

The approach used for this project was focused on the scattering of ultrasound from the grains within the rail and the resulting changes that occurred when the rail was subjected to an applied stress. Although some research in the past has observed changes in scattering due to changes in stress, a thorough and robust quantitative analysis of the scattering process has not been completed previously. In addition, a quantitative approach for this project required that the

complete measurement system be included in the analysis, so that all factors could be considered with respect to their influence on the measured signals.

1.4 Organization of the Report

This report is organized to clarify the model and the corresponding analysis, to detail the experiments pursued, and to highlight the conclusions reached. In Section 2, the basic concepts of diffuse ultrasonic backscatter are described, and a theoretical description is given as the scattering is defined within the context of the complete measurement system, and the model is compared with experimental results. In addition, analysis and experiments are described for both a pulse-echo measurement configuration (with the transducer oriented normal to the sample surface) and a pitch-catch measurement configuration (with one transducer oriented obliquely to the sample surface). In Section 3, the fundamentals of acoustoelasticity and its effect on ultrasonic scattering are described, the importance of the different measurement configurations with respect to the applied stress is demonstrated, and sample results are presented. In Section 4, the application of the ultrasonic scattering methods for stress monitoring is presented, and several laboratory and field experiments are reported. In Section 5, a summary of this report is given, several conclusions are stated, and prospects for future research are presented.

2. Diffuse Ultrasonic Backscatter

In this section, the theoretical model for the diffuse predictions, also described in Section 3, provides the impetus for associated experiments to examine the dependence of diffuse ultrasonic backscatter on applied stress. Those results show that the changes predicted with stress are dependent on the particular measurement mode—a pulse-echo backscatter measurement corresponds with a longitudinal-to-longitudinal (LL) form of scattering, while a pitch-catch measurement is necessary for the mode conversion, or longitudinal-to-transverse (LT), scattering. In this section, and in Section 3, the theoretical foundations for these measurements are presented with respect to the stress measurements described in Section 4.

2.1 Longitudinal-to-Longitudinal Backscatter

A singly-scattered response (SSR) has been derived for LL scattering at normal incidence, based on the more general SSR formulation developed by Ghoshal et al. (2007). The assumption was made that the incident wave scatters only once in the time between excitation and detection. The general expression of the SSR, not limited to LL scattering, was given as:

$$\Phi(t) = \gamma^2 \int \frac{d\omega}{(2\pi)^2} d^3s d^3p d^3q dt' W^R_{\beta j}(\mathbf{x}, t-t', \mathbf{s}, \omega)\, {}^{\mathbf{s}}_{\mathbf{s}}{}^{\beta}_{j}K^{\gamma}_{k}{}^{\mathbf{p}}_{\mathbf{p}} W^S_{jk}(\mathbf{x}, t', \mathbf{p}, \omega) \tag{1}$$

where the parameter γ is now included to provide a conversion between the displacement field and the transducer voltage. The γ parameter is necessary for calibration of experiments. Equation (1) is a double convolution of the Wigner distribution tensors of the source field and the receiver field ($\mathbf{W}^S$, $\mathbf{W}^R$), with an entity that quantifies the microstructure of the material ($\mathbf{K}$). At the simplest level, one can consider Equation (1) as representing an integral of all possible energy states that travel from the source transducer (represented by $\mathbf{W}^S$); scatter once from the microstructure (through $\mathbf{K}$); and are received by the receiving transducer (represented by $\mathbf{W}^R$). Specifically, the intensity operator $\mathbf{K}$ is an eighth-rank tensor that quantifies the second-order spatial statistics of the fluctuations of the elastic moduli (Weaver, 1990), which can be written as:

$${}^{\mathbf{s}}_{\mathbf{s}}{}^{\beta}_{j}K^{\gamma}_{k}{}^{\mathbf{p}}_{\mathbf{p}} \approx \tilde{\eta}(\mathbf{s}-\mathbf{p})\mathbf{s}_{\alpha}\mathbf{p}_{\delta}\mathbf{s}_{l}\mathbf{p}_{m}\Xi^{\alpha\delta\beta\gamma}_{lmjk} = s^2 p^2 \tilde{\eta}(s\hat{\mathbf{s}} - p\hat{\mathbf{p}})\hat{s}_{\alpha}\hat{p}_{\delta}\hat{s}_{l}\hat{p}_{m}\Xi^{\alpha\delta\beta\gamma}_{lmjk} \tag{2}$$

The intensity operator is written assuming the spatial and tensorial components are independent of each other (Weaver, 1990). The function $\tilde{\eta}(\mathbf{s}-\mathbf{p})$ is the spatial Fourier transform of the two-point spatial correlation function. Here, an exponential spatial correlation function is assumed, such that $\eta(r) = \exp(-r/L)$, where L is a spatial correlation length.

The correlation function is the probability that any two points separated by a distance L lie in the same crystal. The tensorial component is the covariance of the elastic moduli given by $\Xi^{\alpha\delta\beta\gamma}_{lmjk} = \langle C_{ijkl} C_{\alpha\delta\beta\gamma} \rangle - \langle C_{ijkl} \rangle \langle C_{\alpha\delta\beta\gamma} \rangle$. This quantity, specified later for a cubic polycrystalline medium, represents the statistics of the spatial distribution of crystal orientations that is responsible for the scattering. The interface of two crystals will have an impedance mismatch due to the grain misalignment. Furthermore, ${}^{\mathbf{s}}_{\mathbf{s}}{}^{\beta}_{j}K^{\gamma}_{k}{}^{\mathbf{p}}_{\mathbf{p}}$ denotes a wave propagating in the $\hat{\mathbf{p}}$ direction that scatters in the $\hat{\mathbf{s}}$ direction. The indices γ, k and β, j are the components of the

displacement vectors associated with the Wigner distribution tensors $W_{\gamma k}^{S}$ and $W_{\beta j}^{R}$.

$W_{\gamma k}^{S}(\mathbf{x},t',\mathbf{p},\omega)$ represents the signal in the space-time domain (represented by displacement vector $\mathbf{x}$ and time t') and the wave vector-frequency domain (represented by wave vector $\mathbf{p}$ and ω) simultaneously.

For a pulse-echo measurement, the forms for the Wigner distribution tensors of the receiver and source fields (assuming longitudinal propagation only) are given by:

$$W_{\beta j}^{R}(\mathbf{x},\mathbf{s},t,\omega) = A_0^2 T_{Lf}^2 (2\pi)^4 \frac{w_0^2}{w_1(z)w_2(z)} \exp\left[-\frac{2x^2}{w_1^2(z)} - \frac{2y^2}{w_2^2(z)} - 2\left(\frac{t}{\sigma}\right)^2\right] \times \exp\left[-\frac{2z(z-2c_L t)}{\sigma^2 c_L^2} - 2\alpha_L z\right] \delta(\mathbf{s}-\mathbf{s}_0)\delta(\omega-\omega_0)\hat{s}_\beta \hat{s}_j (\hat{\mathbf{s}}\cdot\hat{\mathbf{n}})^2,$$

and (3)

$$W_{\gamma k}^{S}(\mathbf{x},\mathbf{p},t,\omega) = A_0^2 T_{fL}^2 (2\pi)^3 \sqrt{2\pi}\sigma \frac{w_0^2}{w_1(z)w_2(z)} \exp\left[-\frac{2x^2}{w_1^2(z)} - \frac{2y^2}{w_2^2(z)} - 2\left(\frac{t}{\sigma}\right)^2\right] \times \exp\left[-\frac{1}{2}\sigma^2(\omega-\omega_0)^2 - \frac{2z(z-2c_L t)}{\sigma^2 c_L^2} - 2\alpha_L z\right] \delta(\mathbf{p}-\mathbf{p}_0)\hat{p}_\gamma \hat{s}_k (\hat{\mathbf{p}}\cdot\hat{\mathbf{n}})^2,$$

with $A_0 = -\exp(-\alpha_f z_f)/4\pi w_0^2 \rho_f c_f^2 \sigma k_f \sqrt{\pi}$ and the phase terms deduced accordingly. Here the phase is not given explicitly, although it is relevant in the later approximations. The complex Gaussian beam parameters are defined by:

$$\begin{aligned}
\frac{1}{q(z)} &= \frac{1}{R(z)} - i\frac{2}{k_f w^2(z)}, \\
q_1(z) &= \frac{q(0)+z_f}{1+\kappa_1(1-c_f/c_L)(q(0)+z_f)} + \frac{c_L}{c_f}z, \\
q_2(z) &= \frac{q(0)+z_f}{1+\kappa_2(1-c_f/c_L)(q(0)+z_f)} + \frac{c_L}{c_f}z,
\end{aligned} \tag{4}$$

where κ_1 and κ_2 are the curvatures of the sample surface. The axial distance z is along the propagation axis of the propagating wave. The Gaussian beam widths can be written as:

$$w_1^2(z) = \frac{-2}{k_f \,\mathrm{Im}(1/q_1(z))}, \quad w_2^2(z) = \frac{-2}{k_f \,\mathrm{Im}(1/q_2(z))}, \tag{5}$$

and the radii of curvature of the wavefront are:

$$R_1(z) = \frac{1}{\mathrm{Re}(1/q_1(z))}, \quad R_2(z) = \frac{1}{\mathrm{Re}(1/q_2(z))}. \tag{6}$$

The initial beam width is the transducer radius $w(0) = w_0$, and the initial radius of curvature of the wavefront is the focal length in fluid $R(0) = -F$. When $\kappa_1 = \kappa_2$, the beam spot at the surface of the solid is circular; otherwise it is an elliptical spot.

It also should be noted that $T_{Lf} = T_{fL}(2\rho_f c_f)/(\rho c_L)$, in which T_{fL} is the transmission coefficient of the longitudinal wave from the fluid to the sample, and T_{Lf} is the transmission coefficient of the longitudinal wave from the sample back to the fluid. The subscripts f and L are used for fluid and sample properties, respectively. c_f is the speed of sound of the fluid; $k_f = \omega_0 / c_f$ is the wave number; α_f and α_L are the attenuation coefficients of the fluid and sample; ρ_f is the fluid density; ω_0 is the center frequency of the input wave; and σ is the width of the input wave in the time domain. Equation (3) indicates that the Wigner transform of the Gaussian beam is a Gaussian function in both space and time (and likely wave vector and frequency, if less restrictive assumptions were invoked). Physically, it is assumed that the majority of the energy of the wave is in the primary propagation direction, which is invoked by using $\delta(\mathbf{s} - \mathbf{s}_0)$ and $\delta(\mathbf{p} - \mathbf{p}_0)$ for both the receiver and the source.

In order to examine the impact of sample curvature on the Wigner transform, the portion of Equation (3) that contains the space and time dependence can be identified. It is given by:

$$A_W(x, y, z, t) = \frac{w_0^2}{w_1(z) w_2(z)} \exp\left[-\frac{2x^2}{w_1^2(z)} - \frac{2y^2}{w_2^2(z)} - 2\left(\frac{t}{\sigma}\right)^2 - \frac{2z(z - 2c_L t)}{\sigma^2 c_L^2} - 2\alpha_L z \right] \quad . \qquad (7)$$

Along the propagation axis ($x = y = 0$), this expression becomes:

$$A_W(0, 0, z, t) = \frac{w_0^2}{w_1(z) w_2(z)} \exp\left[-2\left(\frac{t}{\sigma}\right)^2 - \frac{2z(z - 2c_L t)}{\sigma^2 c_L^2} - 2\alpha_L z \right] \quad , \qquad (8)$$

which describes the amplitude of the Wigner transform of the source along the z axis.

The influence of sample curvature on Equation (8) is examined as follows:

A schematic of a transducer beam propagating through different types of curved interfaces for a given water path is shown in Figure 1. When viewed from the point of view of the transducer, $\kappa < 0$ corresponds to a concave surface, while $\kappa > 0$ represents a convex surface. Note that the in-plane curvature (κ_1) and the out-of-plane curvature (κ_2) can be different. A spherical surface has $\kappa_1 = \kappa_2$ (concave or convex), and a cylindrical surface has one of κ_1 or κ_2 equal to zero. A planar surface implies $\kappa_1 = \kappa_2 = 0$.

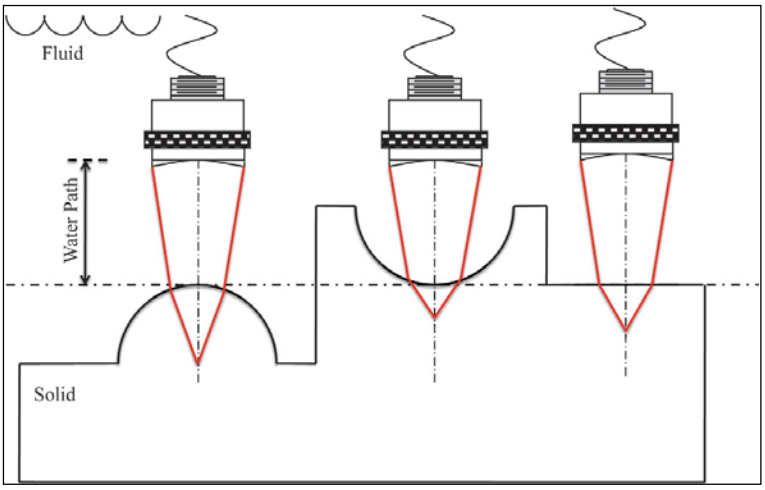

Figure 1. Schematic Showing the Impact of Interface Curvature on Focal Length in the Solid for Identical Water Paths

Assumes concave ($\kappa > 0$), convex ($\kappa < 0$), and planar interfaces.

Examples are now shown with respect to their impacts on Equation (8). The contour of the field from Equation (8) is shown in Figure 2 for aluminum ($c_L = 5973$ m/s and $\alpha_L = 4.05$ Np/m for a 15-MHz input wave) with different curvatures. The speed of sound in water and the water path are 1489 m/s and 50 mm, respectively. The assumed focal length and element diameter of the transducer are 76.2 mm (3 inches) and 12.7 mm (0.5 inches), respectively. The shaded bar indicates the amplitude value of the contour. (Note the difference in the amplitude scale for each plot.)

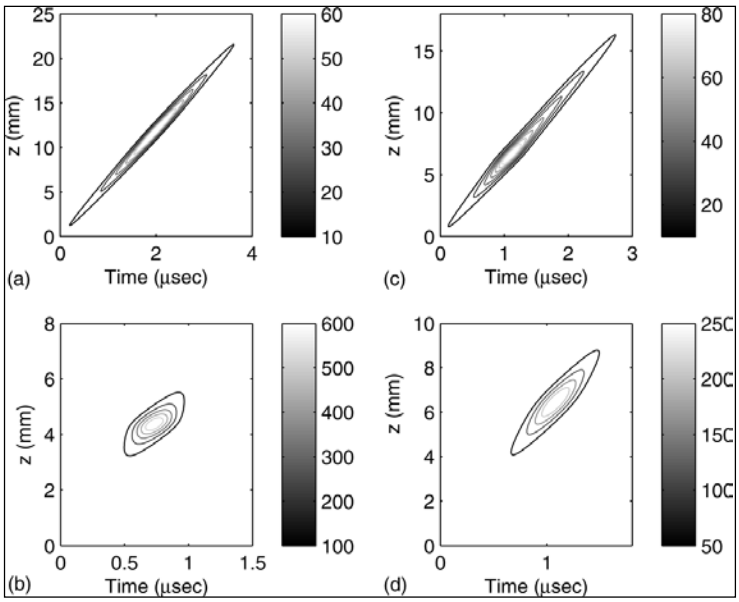

Figure 2. Contour Plot of the Wigner Transform of a Gaussian Beam for Different Curvatures

(a) $\kappa_1 = \kappa_2 = 25\ \text{m}^{-1}$ (concave; spherical). (b) $\kappa_1 = \kappa_2 = -25\ \text{m}^{-1}$ (convex; spherical).

(c) $\kappa_1 = 25\ \text{m}^{-1}, \kappa_2 = 0$ (concave; cylindrical). (d) $\kappa_1 = \kappa_2 = 0$ (planar).

Note that, in some cases, the subplots have very different scales. As expected, the amplitude for all cases is maximum at the focal region and approaches zero away from it. Figures 2(a) and 2(b) represent the Wigner transform amplitude inside a concave ($\kappa_1 = \kappa_2 = 25\,\mathrm{m}^{-1}$) and convex ($\kappa_1 = \kappa_2 = -25\,\mathrm{m}^{-1}$) spherical interface of identical curvature. The impact of the sign of the curvature on the focal depth, focal amplitude, and beam width is clear and highlights the need to consider such effects carefully for comparison with experiments. Figure 2(c) is the Wigner transform amplitude for a cylindrical interface ($\kappa_1 = 25\,\mathrm{m}^{-1}, \kappa_2 = 0$), which when compared with Figure 2(a) shows the impact of the additional curvature out-of-plane. The spherical interface has a narrower beam width, a deeper focus, and a moderately higher amplitude. Finally, Figure 2(d) shows the result for a planar surface, providing another interesting comparison for Figures 2(a)-2(c). In the following section, the LL SSR is derived, using the Wigner transforms defined in Equation (3). The influence of interface curvature on the LL SSR is also illustrated. Subsequently, comparisons are made with experimental results.

Using the definitions of $\mathbf{K}$, $\mathbf{W}^S$ and $\mathbf{W}^R$, the SSR for the LL scattering model can be simplified as:

$$\begin{aligned}\Phi^{LL}(t) = V_{\max}^2 \frac{\pi}{8\sqrt{2}}\left(\frac{w(z_F)}{w_0}\right)^2\left(\frac{\rho c_L^2}{\rho_f c_f^2}\frac{T_{fL}T_{Lf}}{R_{ff}D(\omega_0)}\right)^2\left[\frac{\pi}{2}\frac{\omega_0^4}{c_L^8}\tilde{\eta}(\theta,k_L)\Xi^{\cdots\hat{\mathbf{p}}_0\hat{\mathbf{p}}_0\hat{\mathbf{s}}_0\hat{\mathbf{s}}_0}_{\cdots\hat{\mathbf{p}}_0\hat{\mathbf{p}}_0\hat{\mathbf{s}}_0\hat{\mathbf{s}}_0}(\theta)\right] \\ \times\exp\left(4\alpha_f z_F - 4\alpha_f z_f\right)\exp\left(-\frac{t^2}{\sigma^2}\right)\int_0^\infty \frac{w_0^2}{w_1(z)w_2(z)}\exp\left[-4\alpha_L z - \frac{4z(z-tc_L)}{\sigma^2 c_L^2}\right]dz,\end{aligned} \tag{9}$$

Equation (9) provides a means of connecting the recent scattering theory with experiments involving fluid-solid interfaces. The LL SSR can be subdivided into three major parts: Experimental parameters are shown in $\left(V_{\max}^2 \frac{\pi}{8\sqrt{2}}\left(\frac{w(z_F)}{w_0}\right)^2\left(\frac{\rho c_L^2}{\rho_f c_f^2}\frac{T_{fL}T_{Lf}}{R_{ff}D(\omega_0)}\right)^2\right)$; the diffuse backscatter coefficient, which is proportional to the microstructural properties, is shown in $\left((\pi/2)(\omega_0^4/c_L^8)\tilde{\eta}(\theta)\Xi^{\cdots\hat{\mathbf{p}}_0\hat{\mathbf{p}}_0\hat{\mathbf{s}}_0\hat{\mathbf{s}}_0}_{\cdots\hat{\mathbf{p}}_0\hat{\mathbf{p}}_0\hat{\mathbf{s}}_0\hat{\mathbf{s}}_0}(\theta)\right)$; and lastly, the transducer beam characteristics are given by the remaining terms. The goal of most experiments is to quantify the transducer properties with sufficient accuracy so that Equation (9) can be used to determine microstructural information.

The spatial Fourier transform of the correlation function for longitudinal to longitudinal mode scattering (with scattering angle $\theta = \pi$) is given by Weaver (1990).

$$\tilde{\eta}(\pi,k_L) = \frac{L^3}{\pi^2\left(1+k_L^2L^2\right)^2}, \tag{10}$$

Where k_L is the wave number, and L is the spatial correlation length. The covariance of the elastic moduli for a material with cubic symmetry is given by Weaver (1990), as shown in Equation 11:

$$\Xi^{\cdots\hat{\mathbf{p}}_0\hat{\mathbf{p}}_0\hat{\mathbf{s}}_0\hat{\mathbf{s}}_0}_{\cdots\hat{\mathbf{p}}_0\hat{\mathbf{p}}_0\hat{\mathbf{s}}_0\hat{\mathbf{s}}_0}(\theta) = \frac{\nu^2}{\rho^2}\left[\frac{9}{525} + \frac{6}{525}\cos^2\theta + \frac{1}{525}\cos^4\theta\right], \tag{11}$$

where $\nu = c_{11} - c_{12} - 2c_{44}$, and $\theta = \pi$, as discussed previously. For a fine-grained steel, the single-crystal material properties and density are assumed to be: $c_{11} = 219.2\,\text{GPa}$, $c_{12} = 136.8\,\text{GPa}$, $c_{44} = 109.2\,\text{GPa}$, and $\rho = 7700\,\text{kg/m}^3$. To highlight the effects of the interface curvature on the LL SSR, an amplitude term—denoted by A_Φ—is defined from Equation (9) as:

$$A_\Phi(t) = \exp\left(-\frac{t^2}{\sigma^2}\right)\int_0^\infty \frac{w_0^2}{w_1(z)w_2(z)}\exp\left[-4\alpha_L z - \frac{4z(z-tc_L)}{\sigma^2 c_L^2}\right]dz, \tag{12}$$

where all other parameters in Equation (9) are not related to the curvature. Numerical results of the amplitude for various interface curvatures are shown in Figure 3 (a 30-mm water path is assumed; all other parameters are identical to those used for Figure 2).

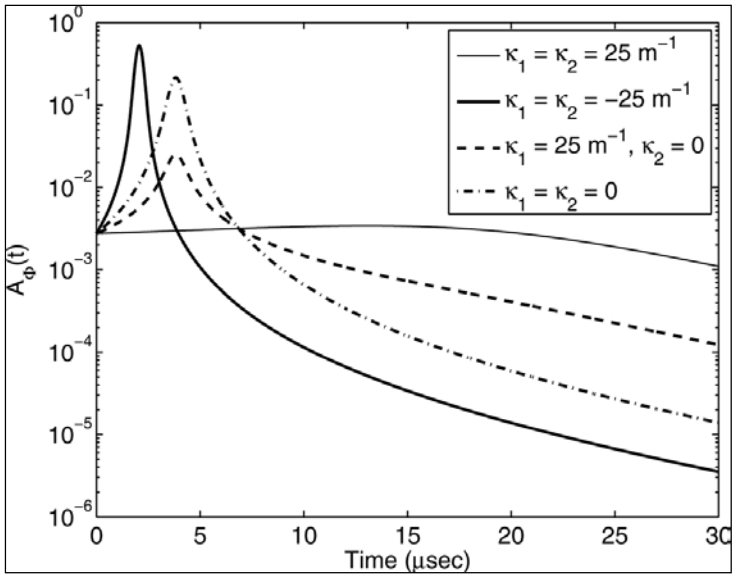

Figure 3. Theoretical Diffuse Backscatter Amplitude as a Function of Time for Different Interface Curvatures, With All Other Parameters Held Constant

The LL SSR curves display characteristics expected from the convolution of the two Wigner transforms plotted in Figure 2. A convex curvature diverges the beam such that a deeper focus is created. Hence, the amplitude with the minimum energy is observed for the curvature with $\kappa_1 = \kappa_2 = 25\,\text{m}^{-1}$ shown. The earliest peak arrival time and the maximum amplitude are observed for a concave curvature ($\kappa_1 = \kappa_2 = -25\,\text{m}^{-1}$), due to the enhanced focusing in the material induced by the curvature. The results for $\kappa_1 = 25\,\text{m}^{-1}, \kappa_2 = 0$, and $\kappa_1 = \kappa_2 = 0$ represent cylindrical and planar interfaces, respectively. The cylindrical curvature reduces the peak amplitude in comparison with the planar interface, but the influence on the focal depth is minimal for the cases studied here. Thus, it is clear that the expression given by Equation (3) forms a key component of such diffuse field predictions. In the next section, this importance is also evident when experimental results are fit using the theoretical model in Equation (9).

Experimental results are now presented and compared with the theoretical model. The quantity derived above is the spatial variance of the signals acquired from a typical ultrasonic C-scan. A schematic illustration of such an experiment is shown in Figure 4. A sample of thickness d is

assumed, with the circular spots used to indicate the various transducer positions typical of such an experiment. (Note that positions near edges are avoided.)

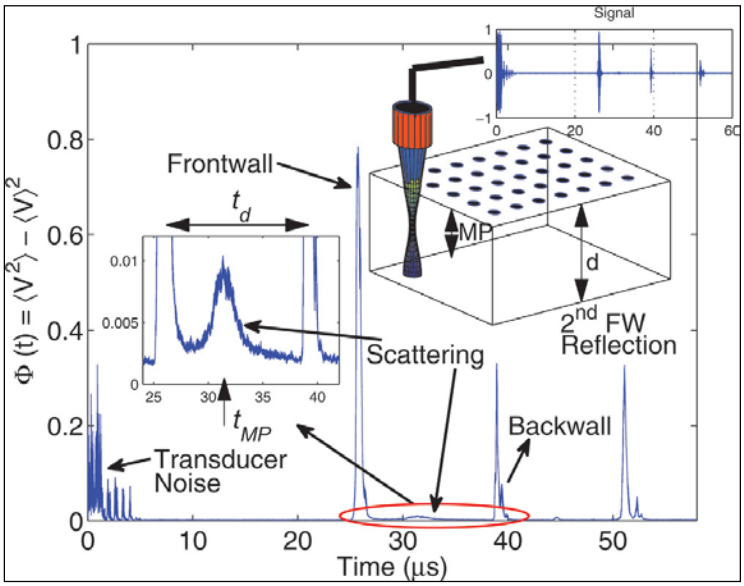

Figure 4. Example of a Diffuse Ultrasonic Experimental Setup

The transducer pulse-echo signal is collected at several different spatial positions. (t_d and t_{MP} are the times required to travel twice the depth of the material and the MP, respectively.) The variance of the signal shows the level of the scattering relative to the front and backwall reflections.

The material path (MP), also known as the geometrical focus, is defined as the focal depth in the test material as shown in Figure 4. The MP is calculated by:

$$MP = (F - WP)\frac{c_f}{c_L}, \tag{13}$$

where WP is the water path distance from the transducer face to the front surface of the planar test sample. This expression is valid for weakly scattering materials, since it does not include any influence due to microstructural scattering.

The variance of all the signals is calculated to obtain the experimental LL SSR. The transducer noise, frontwall reflection, backwall reflection, and second frontwall reflection can be identified easily in the LL SSR by examining any particular single signal, and from knowledge of the sample geometry and longitudinal wave speed. Because the magnitude of the scattered response is small compared with the frontwall or backwall reflection, the variance curve between the frontwall and the backwall reflection is shown at higher magnification in the inset of Figure 4. The LL SSR model developed above is used to fit this curve and extract microstructural properties of the test sample. Note that the electronic noise from the equipment, which can be observed distinctly before the frontwall reflection, is small (by several orders of magnitude) in comparison with the scattered response.

Here the main focus is on extraction of the spatial correlation length L of the microstructure from the experimental results. A rectangular steel block of size $100\text{ mm} \times 40\text{ mm} \times 50\text{ mm}$ was used for these experiments, and a 15-MHz transducer (Panametrics Model V309, from GE Panametrics, Inc., Waltham, MA) with a 76.2-mm (3-inch) nominal focus and 12.7-mm (0.5-inch) element diameter. The transducer was operated in pulse-echo mode using a DPR 300 pulser/receiver (Imaginant and JSR Ultrasonics, Pittsford, NY). The echo signals were recorded and digitized with a 12-bit, 100-MHz analog-to-digital (A/D) card (Physical Acoustics Corporation, Princeton, NJ) and downloaded to a personal computer (PC) for postprocessing. The sampling rate used to digitize the received signals was 250 MHz. In these experiments, the sample was held stationary, and the transducer was moved using a computer-controlled micropositioning system.

Several experimental parameters required for the model first had to be determined (including the peak amplitude $V_{\max}$, the Gaussian beam width in time σ, sound speed in water and in the sample, and attenuation for the fluid and sample), and they all were found in independent experiments. A block of fused silica was used as a reference sample for extraction of $V_{\max}$. These measurements resulted in the following values: $c_L = 5973.1$ m/s, $\alpha_L = 0.0405$ Np/cm, $c_f = 1476.2$ m/s, $\alpha_f = 0.0532$ Np/cm. The attenuation coefficients were determined at 15-MHz input frequency. In addition, the transducer beam pattern was first characterized using a hydrophone (HNV Series, Onda Corporation, Sunnyvale, CA) to map the pressure profile in water such that the focal length and beam width were known. In the subsequent subsections, experimental results for these normal incidence experiments are given for both planar and cylindrical samples.

The experimental setup (shown in Figure 4) was used with a water path of 25 mm (the sample depth in the direction of the wave propagation of 40 mm). Signals from 800 transducer positions were recorded, with at least one wavelength of separation between any two consecutive transducer positions. Thus, all signals can be assumed to be uncorrelated. From Equation (4), using $\kappa_1 = \kappa_2 = 0$ for a planar interface, the complex Gaussian beam parameters (Schmerr and Song, 2007) reduce to:

$$q_1(z) = q_2(z) = q(0) + z_f + \frac{c_L}{c_f} z. \tag{14}$$

The calculated spatial variance of the ensemble of signals is shown in Figure 5. The model for the LL SSR was fitted to experimental results, with the spatial correlation length used as the only fitting parameter. (All other quantities were known from the other independent experiments.) The diffuse part of the signal between the frontwall and backwall echoes was used to fit the theoretical model, because the theoretical model does not account for the frontwall and backwall echoes. Using the experimentally obtained LL SSR $\Phi_{\text{EXP}}(t)$ with Equations (9) and (10), the correlation length was determined by solving:

$$L^4 - \left(\frac{\Lambda(t)}{\pi^2 k^4 \Phi_{\text{EXP}}(t)} \right) L^3 + \left(\frac{2}{k^2} \right) L^2 + \frac{1}{k^4} = 0, \tag{15}$$

where $\Lambda(t) = \Phi(t) / \tilde{\eta}(\pi, k)$ and $k = \omega_0 / c_L$.

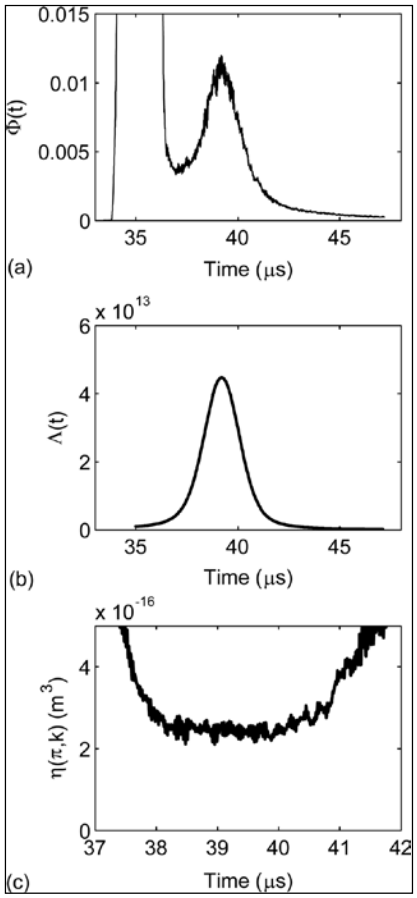

Figure 5. Extraction of Correlation Length from Experimental Data
(a) Experimental result using a 15-MHz focused transducer on a steel sample (average grain size $15.3\ \mu$m) through a planar surface.
(b) Theoretical $\Lambda(t)$. (c) $\tilde{\eta}(\pi,k)$ at respective time points.

Equation (15) has four solutions, but experience with the solution when it is applied to experimental data shows that only one root is physically meaningful. Thus, that root is chosen as the estimated correlation length. Following a simple regression scheme, a correlation length of $L = 15.5 \pm 0.4\ \mu$m is estimated, where the standard deviation is due to the fluctuations in the experimental LL scattering results.

For example, experimental LL SSR and theoretical $\Lambda(t)$ are shown in Figure 5, (a) and (b), respectively. The ratio of (a) to (b), shown in Figure 5 (c), is equal to $\tilde{\eta}(\pi,k)$. Equation (15) is solved for the time window of $38 - 40.2\ \mu$s, which is obtained from the region of the curve shown in Figure 5 (c), where the slope is within $\pm 5^0$ of zero. The theoretical fit using the extracted mean correlation length ($L = 15.5\ \mu$m) is shown in Figure 6 for direct comparison with the experimental results. The experimental curve is fit using the theoretical model in order to extract the spatial correlation length (the fit shown uses $L = 15.5\ \mu$m).

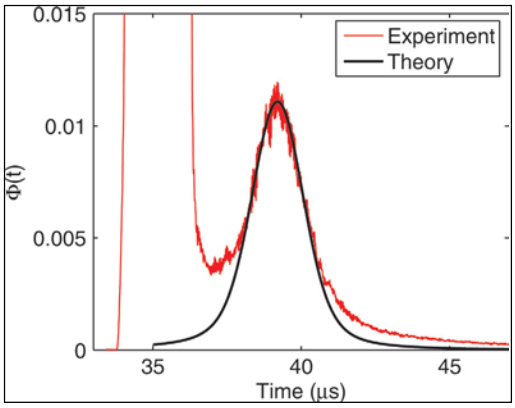

Figure 6. Experimental Result Using a 15-MHz Focused Transducer on a Steel Sample Through a Planar Surface
Average grain size 15.3 μm.

Two points may also be made about the range of validity of the curve fit. At times, before the LL SSR peak, the theoretical curve deviates from the experimental due to the presence of the front wall reflection. Large amplifier gains are typically used for such experiments causing the front wall reflection to exceed the data acquisition amplitude window. Thus, the location of the transducer focus must be deep enough in the sample to avoid these effects if the LL SSR rise is to be captured. Second, there is a deviation from the model at times after the peak (after ~ 41 μs). The theoretical model was developed using assumptions of single scattering such that higher-order scattering effects are not included. These effects, which are expected after the main LL SSR peak, should always be greater than the LL SSR model, as observed here.

The steel sample was machined into a cylindrical sample, so that the ability of the model to capture such a configuration could be explored. Figure 7 is a schematic diagram showing the orientation of the transducer relative to the sample, where the Plane of Incidence (POI) is along the plane containing the diameter (on the x-z plane). The POI contains both the incident wave direction and the normal to the interface. The analytical expression for the LL SSR [shown in Equation (9)] can be used directly, but the complex Gaussian beam parameters must be modified to account for the interface geometry. The complex Gaussian beam parameters for the cylindrical interface (Schmerr and Song, 2007) are written as:

$$q_1(z) = \frac{q(0)+z_f}{1+\kappa\left(1-c_f/c_L\right)\left(q(0)+z_f\right)} + \frac{c_L}{c_f}z,$$
$$q_2(z) = q(0)+z_f+\frac{c_L}{c_f}z, \tag{16}$$

where κ is the curvature of the cylinder ($\kappa = 1/R$, where R is the cylinder radius). The radius of curvature can be nondimensionalized by the initial beam width such that the quantity $\varpi = \kappa w_0$ can be defined. Experiments are carried out using a cylinder of radius $R = 40.2$ mm ($\kappa = 24.87$ m^{-1}, $\varpi = 0.158$) and height 120 mm. Ultrasonic signals are captured from 800 transducer positions after carefully aligning the transducer along the POI. The transducer parameters and general experimental procedure are identical to those used for the planar interface.

The experimental LL SSR is shown in Figure 7 for a water path of 45 mm. The experimental SSR is fit over a time range of 64.5 to 68 μs, following a similar technique used for the planar interface case. Solving Equation (15), a correlation length of $L = 16.1 \pm 0.7$ μm is estimated. The comparison of the theoretical model using the extracted mean correlation length ($L = 16.1$ μm), with the experimental LL SSR is shown in Figure 8. The value of L for the cylindrical interface is slightly larger than that extracted from the planar interface. Although the difference is small (less than 4%), the reason for the difference is not clear at this point. It is thought to be due to the use of the Gaussian beam model, which is known to have limitations (Schmerr and Song, 2007) and may result in such a systematic bias in the value of the correlation length. It is also observed that the theoretical model fits well at early times and deviates from the experimental data at later times. In this case, the theoretical curve lies above the experimental curve, suggesting that the model for this system may need to be improved (again, possibly due to the Gaussian beam model).

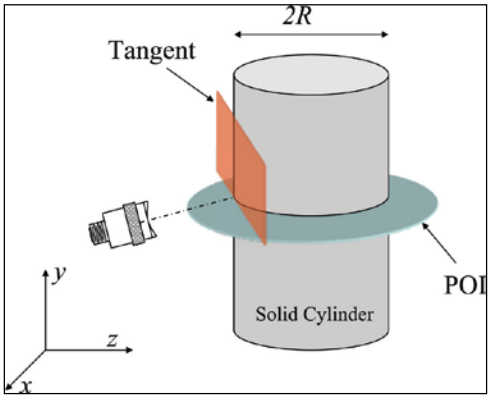

Figure 7. Schematic of the Ultrasonic Experimental Setup for Measurements on Cylindrical Samples

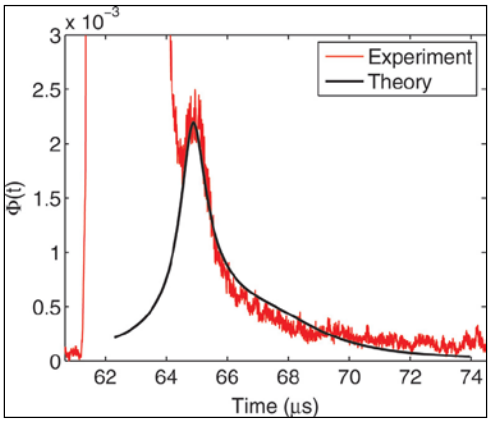

Figure 8. Experimental Result Using a 15-MHz Focused Transducer on a Steel Sample (Average Grain Size 15.3 μm) Through a Cylindrical Surface

Experimental curve is fit using the theoretical model in order to extract the spatial correlation length. The best fit shown uses $L = 16.1$ μm.

2.2 Longitudinal-to-Transverse Backscatter

Scattering effects typically are observed when experiments are designed using frequencies with corresponding wavelengths on the order of the heterogeneity length scale. In metallic specimens, this length scale corresponds to the grain size. The scattering that occurs at grain boundaries includes both longitudinal and transverse wave components because of the continuity conditions at the interfaces. The mode-converted LT scattering can be observed by utilizing a pitch-catch transducer configuration, in which the receiving transducer is oriented above the first critical angle such that the scattered transverse energy is captured.

In this report, the configuration is restricted to the case of LT scattering only (as shown schematically in Figure 9), for which the source transducer excites a longitudinal wave, and the receiving transducer captures the transverse wave (the reciprocal case is equivalent). For this configuration, the foci of the transducers are chosen to overlap at a desired depth O in the material. The water and material paths, z_{fS} (and z_{fR}) and z_S (and z_R), are properly chosen to achieve this overlap for a given material, because these paths depend on the wave speeds in the material. The subscripts S and R distinguish the transducer types for the respective source and receiver.

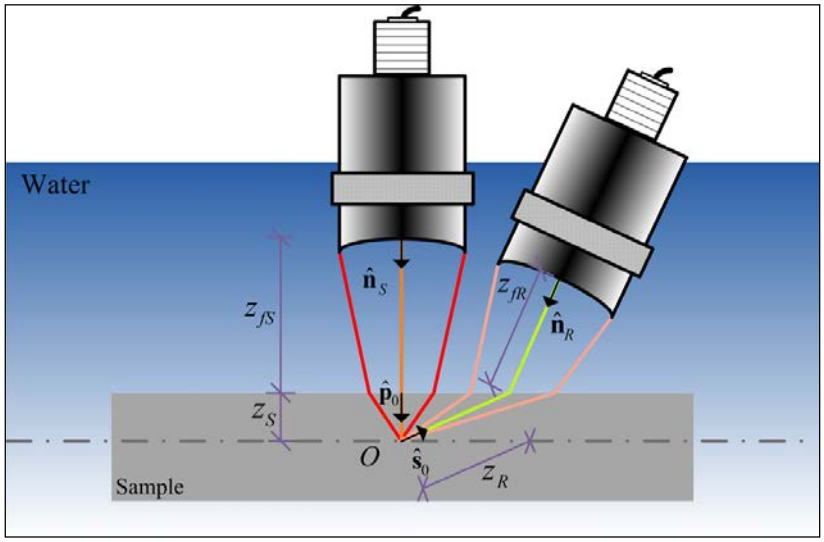

Figure 9. Schematic Diagram of a Pitch-Catch Transducer Configuration
The left transducer acts as source and the right (oblique) transducer as receiver.

In contrast to the LL model, here the source and receiver coordinates, $\mathbf{x}$ and $\mathbf{X}$, are no longer the same for the pitch-catch configuration of interest. Thus, the corresponding single-scattering LT model is first modified from Equation (1) as:

$$\Phi^{LT}(t) = \gamma_S \gamma_R \int \frac{d\omega}{(2\pi)^2} d^3s d^3p d^3q dt' W^R_{\beta j}(\mathbf{x}, t-t', \mathbf{s}, \omega)^{\mathbf{s}}_{\mathbf{s}}{}^{\beta}_{j} K^{\gamma}_{k}{}^{\mathbf{p}}_{\mathbf{p}} W^S_{\gamma k}(\mathbf{x}, t', \mathbf{p}, \omega), \qquad (17)$$

where each Wigner distribution function is written with respect to its own local coordinate. Then $\mathbf{X}$ can be expressed with respect to $\mathbf{x}$ using a coordinate transformation. The Wigner distribution function of the normal incidence source transducer ($\mathbf{W}^S$) remains the same as in the

LL model, because its coordinates are used as the global coordinates (Ghoshal and Turner, 2010), as shown in the second expression of Equation (3). It is given explicitly as:

$$W_{jk}^{S}(\mathbf{x},\mathbf{p},t,\omega) = A_{0S}^2 T_{jL}^2 (2\pi)^3 \sqrt{2\pi}\sigma_S \frac{w_{0S}^2}{w_1(z)w_2(z)} \exp\left[-\frac{2x^2}{w_1^2(z)} - \frac{2y^2}{w_2^2(z)} - 2\left(\frac{t}{\sigma_S}\right)^2\right] \times \exp\left[-\frac{1}{2}\sigma_S^2(\omega-\omega_0)^2 - \frac{2z(z-2c_L t)}{\sigma_S^2 c_L^2} - 2\alpha_L z\right] \delta(\mathbf{p}-\mathbf{p}_0)\hat{p}_\gamma \hat{s}_k (\hat{\mathbf{p}}\cdot\hat{\mathbf{n}}_S)^2. \tag{18}$$

Here, A_{0S}, σ_S, w_{0S} and $\hat{\mathbf{n}}_S$ are used to replace the original A_S, σ, w_0 and $\hat{\mathbf{n}}$, respectively, in which the additional subscript S is used especially for the source transducer, and the physical meanings remain the same as explained above. Accordingly, the single Gaussian beam model is given as:

$$\begin{aligned} \frac{1}{q_\xi(z)} &= \frac{1}{R_\xi(z)} - i\frac{2}{k_f w_\xi^2(z)}, \\ q_{1\xi}(z) &= \frac{\cos^2\theta_r}{\cos^2\theta_i}\left[q_\xi(0) + z_{f\xi}\right] + \frac{c_\chi}{c_f} z, \\ q_2(z) &= q_\xi(0) + z_{f\xi} + \frac{c_\chi}{c_f} z, \end{aligned} \tag{19}$$

where the subscript ξ is used to discriminate the transducers, $\xi = S, \mathrm{R}$ (source and receiving transducers)—i.e., $z_{f\xi}$ is the water path for the ξ transducer. $R_\xi(0) = -F$ and $w_\xi(0) = w_{0\xi}(0) = 07517a$ are the initial radius and beam width of the wavefront, respectively, for which F is the focal length of the transducer in water and a is the nominal radius of the transducer (Thompson and Lopes, 1984). The subscript χ is used to distinguish the wave types. where $\chi = L, R$ (longitudinal and transverse wave), and c_χ is the corresponding wave speed. z is the axial distance along the propagation direction. The last terms contain the ratio of material to fluid wave speeds. These terms are necessary in order to define the Gaussian beam properly over the fluid and sample in Figure 9, and the ratio of wave speeds is used to convert all the variables with respect to the fluid instead of the sample (Schmerr, 2000). Finally, θ_i and θ_r are the angles of incidence and refraction, respectively, of the oblique transducer shown in Figure 10.

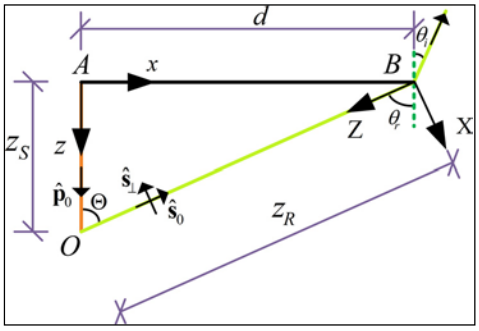

Figure 10. Geometrical Relationship for Coordinate Transformation

From these definitions, the widths of the single Gaussian beam (Ghoshal and Turner, 2010; Ghoshal et al., 2007) are found as:

$$w_1^2(z) = \frac{-2}{k_f \,\mathrm{Im}\left(1/q_{1\xi}(z)\right)}, \quad w_2^2(z) = \frac{-2}{k_f \,\mathrm{Im}\left(1/q_{2\xi}(z)\right)}, \tag{20}$$

and the radii of curvature of the wavefront are:

$$R_1(z) = \frac{1}{\mathrm{Re}\left(1/q_{1\xi}(z)\right)}, \quad R_2(z) = \frac{1}{\mathrm{Re}\left(1/q_{2\xi}(z)\right)}, \tag{21}$$

For a planar sample surface, the Gaussian beam widths are equal at normal incidence: $w_1(z) = w_2(z) = w(z)$. However, at oblique incidence, $w_1(z) \neq w_2(z)$. The complete integration required in Equation (17) for the LT scattering model requires first a clear understanding of the Wigner distribution function of the receiver oriented at oblique incidence. The basic definitions given for the normal incidence expression in Equations (18), (19), (20) and (21) provide the necessary basis for this derivation.

Now, consider the longitudinal propagation path $\mathbf{x}$ as the global material coordinate, such that the transverse wave path $\mathbf{X}$ is initially defined in a local coordinate system. Then, $\mathbf{X}$ may be written with respect to $\mathbf{x}$ based on a coordinate transformation. The origin of the former coordinate is A and the latter B (as shown in Figure 10). Both are on the surface of the sample, and the separation distance $d = z_S \cdot \tan\Theta$ is constant for a given angle of incidence. Thus, $|AO| = z_S$ and $|BO| = z_R$ correspond to the respective material paths. The angle between them is Θ, which is equal to the angle of refraction of the transverse wave, i.e., $\Theta = \theta_r$.

The necessary coordinate transformations are defined as:

$$\begin{cases} X = x\cos\Theta + z\sin\Theta - d\cos\Theta, \\ Y = y, \\ Z = -x\sin\Theta + z\cos\Theta + d\sin\Theta, \end{cases} \tag{22}$$

The Wigner distribution function of the receiver field is first expressed in its local coordinates (i.e., $x \to X$, $y \to Y$, $z \to Z$) and by replacing the longitudinal with the transverse parameters $c_L \to c_T, \alpha_L \to \alpha_T, \mathbf{p} \to \mathbf{s}$ and $\hat{\mathbf{n}}_S \to \hat{\mathbf{n}}_R$ in Equation (18). It is also convenient to use the delta function form for the frequency dependence (Carrier et al., 1983). In addition, the polarization of the scattered transverse wave that ultimately converts in the fluid for detection is defined as $\hat{\mathbf{s}}_\perp$, as shown in Figure 10. Thus, the Wigner distribution function for the receiving transducer becomes:

$$\begin{aligned} W_{\beta j}^R(\mathbf{x},\mathbf{s},t,\omega) = A_{0R}^2 T_{Tf}^2 (2\pi)^4 \frac{w_{0R}^2}{w_1(Z)w_2(Z)} \exp\left[-\frac{2X^2}{w_1^2(Z)} - \frac{2Y^2}{w_2^2(Z)} - 2\left(\frac{t}{\sigma_S}\right)^2 \right] \\ \times \exp\left[-\frac{2Z(Z - 2c_T t)}{\sigma_S^2 c_T^2} - 2\alpha_T Z \right] \delta(\mathbf{s} - \mathbf{s}_0)\delta(\omega - \omega_0)\hat{s}_{\perp\beta}\hat{s}_{\perp j}(\hat{\mathbf{s}} \cdot \hat{\mathbf{n}}_S)^2, \end{aligned} \tag{23}$$

for which the center frequency of the receiving transducer is assumed to match the source frequency input, ω_0 (an assumption that could be relaxed in future work).

In Equation (23), T_{Tf} is the transmission coefficient of the transverse wave from the sample to water, and α_T is the transverse attenuation of the sample. $\hat{\mathbf{n}}_S$ and $\mathbf{s}_0$ are, respectively, the unit normal in the axial direction of the receiving transducer, and the wave vector along the material path of the receiving transducer ($\hat{\mathbf{s}}_0$) in Figure 10. Therefore, Equations (18) and (23) are the Wigner distribution functions of the normal incidence and oblique incidence transducers, respectively, with each defined in its own coordinate system. Note that A_{0R} differs from A_{0S} above only with respect to the propagation path and transducer properties.

Next, the coordinate transformation is utilized by substituting Equation (22) into Equation (23), such that $\mathbf{W}^S$ and $\mathbf{W}^R$ are referenced to the same coordinate system. The effect of the incidence angle on the spatial and temporal distributions of energy can be examined through the terms in $\mathbf{W}^S$ and $\mathbf{W}^R$ with space ($\mathbf{x}$) and time (t) dependence.

Similar to the LL model, the dimensionless spatial and temporal distributions of spectral energy for the source and receiving transducers are denoted as A_{W^S} and A_{W^R}, which quantify the spreading of the beam in the material as a function of incident angle—all within the limitations of the single Gaussian beam assumption. For increasing angle of incidence, the beam cross-section becomes more elliptical in shape. The influence of the angle of incidence on the beam shape can be visualized by using a simple example based on A_{W^S} and A_{W^R} (Figure 11), where the color bar displays the amplitude of the corresponding image.

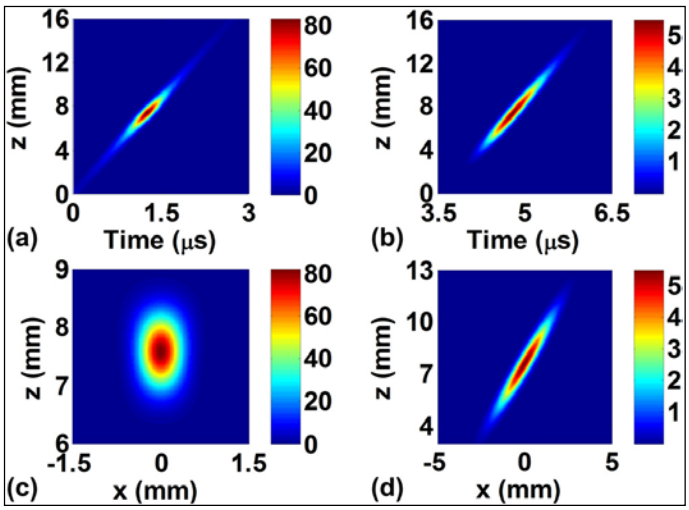

Figure 11. Angular Dependence of the Wigner Distribution Function of a Gaussian Beam on a Planar Interface

(a) A_{W^S} with $x = y = 0$ (the beam profile along the propagation axis).
(b) A_{W^R} with $x = y = 0$ (the beam profile along the propagation axis).
(c) A_{W^S} with $y = 0$ and $t_1 = z_S / c_L$ (a slice of the beam cross-section).
(d) A_{W^R} with $y = 0$ and $t_2 = z_R / c_T$ (a slice of the beam cross-section)

For this example calculation, both transducers are assumed to be focused transducers with a central frequency $\omega_0 = 2\pi \times 10$ MHz, focal length $F = 50.8$ mm, pulse width $\sigma_S = 0.16\ \mu$s, and transducer nominal element diameter $D = 12.7$ mm. The sample is assumed to be steel with $\rho = 7880$ kg/m^3 m/s, $c_L = 5902$ m/s, $c_T = 3164$ m/s, $\alpha_L = 5.83$ Np/m, and $\alpha_T = 24.35$ Np/m. The coupling fluid is assumed to be water with $\rho_f = 998.2$ kg/m^3, and $c_f = 1486$ m/s. The water path $z_{fS} = 20.5$ mm is for the normal incidence source transducer, and the path $z_{fR} = 16.9$ mm is for the oblique receiving transducer. The angle of the oblique incidence transducer is chosen as $\theta_i = 24^\circ$. The location of the focal point is observed to be at the same location in space for both transducers.

For the case along the propagation axis, $A_{W^S}(0,0,z,t)$ and $A_{W^R}(0,0,z,t)$, as shown in Figure 11(a) and (b), the focal location is the same. However, the arrival time is different due to the different material paths and wave speeds. The cross-section of the beam for $A_{W^S}(x,0,z,t_1)$ and $A_{W^R}(x,0,z,t_2)$ is shown in Figure 11(c) and (d). For the parameters chosen, $t_1 = z_S / c_L$ is the travel time for the longitudinal wave in the sample, and $t_2 = z_R / c_T$ is the travel time for the transverse wave. The beam profile appears circular and elliptical for the normal and oblique incidence transducers, respectively. In addition, it should be noted that the maximum value for the amplitude is almost 20 times different for these two cases. This result certainly will play a role in the expected scattering response for each of the respective experiments. With both the source and receiver Wigner distributions now defined, the full expression for the LT scattering model can be completed.

Using the definitions of $\mathbf{K}$, $\mathbf{W}^S$, and $\mathbf{W}^R$, the SSR for the LT scattering model can be obtained as:

$$\Phi^{LT}(t) = \Phi_0^{LT}(t) B^{LT} \int_0^{\infty} dz \int_{-\infty}^{+\infty} dx \exp\left(-\frac{t^2}{\sigma_S^2}\right) \frac{w_{0S}^2 / \sqrt{w^2(z) + w_2^2(Z)}}{w(z) w_1(Z)} \exp\left[-\frac{2x^2}{w^2(z)} - \frac{2X^2}{w_1^2(Z)}\right]$$
$$\times \exp\left[-\frac{2z^2}{\sigma_S^2 c_L^2} - \frac{2Z^2}{\sigma_S^2 c_T^2} + \frac{4Zt}{\sigma_S^2 c_T} - 2\alpha_L z - 2\alpha_T Z - \frac{1}{\sigma_S^2}\left(\frac{Z}{c_T} - \frac{z}{c_L}\right)^2 - \frac{2t}{\sigma_S^2}\left(\frac{Z}{c_T} - \frac{z}{c_L}\right)\right], \tag{24}$$

with:

$$\Phi_0^{LT}(t) = V_{\max}^S V_{\max}^R \frac{\pi}{8\sqrt{2}} \frac{w(z_{FS}) w(z_{FR})}{w_{0S}^2} \left(\frac{\rho c_L c_T}{\rho_f c_f^2}\right)^2 \frac{\cos^2(\Theta - \theta_i) T_{fL}^2 T_{Tf}^2}{R_{ff}^2 D_S(\omega_0) D_R(\omega_0)} \frac{4\sigma_S}{\sqrt{2\pi}\sigma_R}$$
$$\times \exp\left(2\alpha_f z_{FS} - 2\alpha_f z_{fS} + 2\alpha_f z_{FR} - 2\alpha_f z_{fR}\right), \tag{25}$$

defined as a constant that depends on factors related to the experiment calibration and:

$$B^{LT} = \frac{\pi}{2} \frac{\omega_0^4}{c_L^4 c_L^8} \tilde{\eta}_{LT}(\pi - \Theta) \Xi_{\cdots \hat{\mathbf{p}}_0 \hat{\mathbf{p}}_0 \hat{\mathbf{s}}_0 \hat{\mathbf{s}}_\perp}^{\cdots \hat{\mathbf{p}}_0 \hat{\mathbf{p}}_0 \hat{\mathbf{s}}_0 \hat{\mathbf{s}}_\perp}(\pi - \Theta), \tag{26}$$

defined as the LT diffuse backscatter coefficient, in which the covariance function and the correlation function can also be further reduced if the single crystal symmetry is assumed to be cubic.

In this case:

$$\tilde{\eta}_{LT}(\pi-\Theta)=\frac{L^3}{\pi^2\left[1+L^2\left(k_L^2+k_T^2+2k_Lk_T\cos\Theta\right)\right]^2}, \tag{27}$$

and

$$\Xi^{\cdots\hat{\mathbf{p}}_0\hat{\mathbf{p}}_0\hat{\mathbf{s}}_0\hat{\mathbf{s}}_\perp}_{\cdots\hat{\mathbf{p}}_0\hat{\mathbf{p}}_0\hat{\mathbf{s}}_0\hat{\mathbf{s}}_\perp}(\pi-\Theta)=\frac{\nu^2}{\rho^2}\left(\frac{10}{525}+\frac{\cos^2\Theta}{525}-\frac{\cos^4\Theta}{525}\right), \tag{28}$$

where the wave numbers are referenced to the center frequency of the source transducer in terms of wave speeds, *i.e.*, $k_L=\omega_0/c_L$, $k_T=\omega_0/c_T$. Also, L is the correlation length of the specimen's microstructure, a quantity on the order of the mean grain size, and ν is the anisotropy coefficient defined as in LL SSR model (Weaver, 1990).

To highlight the dependence of the mode-converted backscatter on correlation length L and material paths z_S, several results are shown in Figure 12, assuming a 10-MHz measurement in steel. The responses for $L=20$, 25, and 30 μm are shown in Figure 12(a), for which the LT SSR amplitude is observed to increase with the correlation length as expected. Because of the constant water path, the arrival times of the SSR peaks are the same. Results for various material paths ($z_S=9.0$, 7.7, and 6.4 mm) are shown in Figure 12(b). The material paths correspond with water paths of $z_{fS}=15$, 20, and 25 mm. For these results, the LT SSR amplitude is observed to increase with the reduction of the material path, and the arrival times of the scattering peaks are delayed as the water path increases.

In order to examine the validity of the model, a pitch-catch scattering experiment was designed. The sample was a block of type 1040 steel with dimensions 50.5 mm × 50.6mm × 101.7 mm. The sample was annealed to remove possible residual stresses that may have been present. The density was found to be $\rho=7836\,\text{kg/m}^3$, and the single-crystal material properties of iron were assumed as $c_{11}=219.2\,\text{GPa}$, $c_{12}=136.8\,\text{GPa}$, and $c_{44}=109.2\,\text{GPa}$. The longitudinal and transverse wave speeds in the specimen were experimentally evaluated by cross-correlating two successive back wall echoes reflected from the sample. The former was measured with an immersion transducer, and the latter was determined with a contact transverse transducer. The wave speeds were found to be $c_L=5912$ m/s and $c_T=3235$ m/s, respectively. Optical microscopy was used to determine the mean grain size of a polished specimen taken from the test piece. The grain size from the optical microscopy measurement was used for comparison with the grain size determined from the scattering measurements.

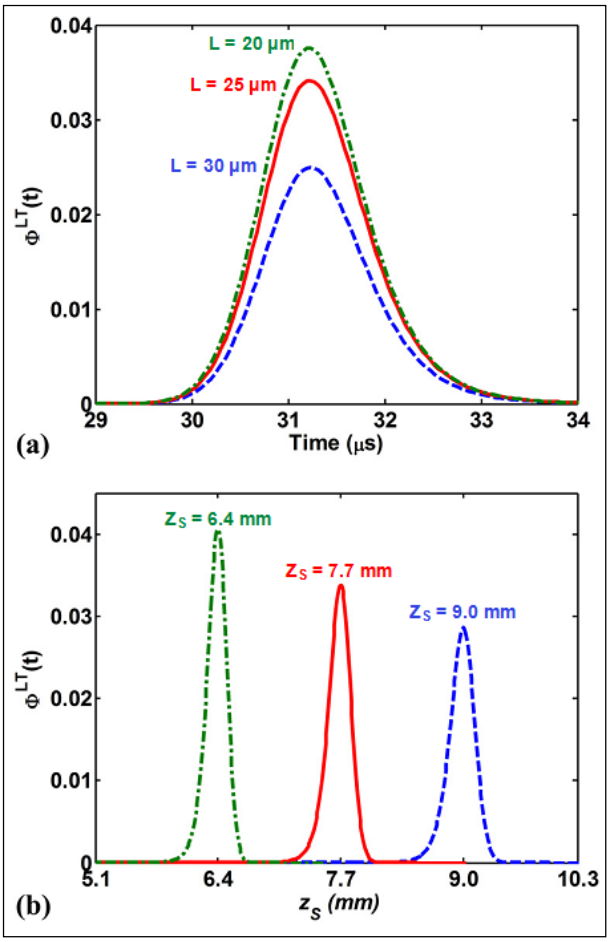

Figure 12. Dependence of Correlation Lengths and Material Paths on the Mode-Converted LT SSR at 10 MHz for the Steel Sample

(a) LT model scattering with various correlation lengths.
(b) LT model scattering with various material paths

From the theoretical LT model given (Equation 24), it is clear that several independent calibration measurements must first be conducted so that the bulk specimen properties and the transducer properties can be quantified. The calibration measurements for $V_{\max}^{S}$ and $V_{\max}^{R}$ were performed on a metallographically polished region of the steel specimen. A steel ball with a diameter of 3.16 mm was used as a reflector to determine the pulse widths σ_S and σ_R along with the central frequency ω_0, and the focal length F of each transducer.

For the experimental setup (Figure 9), two transducers (Panametrics V327, GE Panametrics, Inc., Waltham, MA, with parameters 10 MHz, 50.8-mm point target focus, and 9.525-mm element diameter) were used with a DPR 300 pulser/receiver (Imaginant and JSR Ultrasonics, Pittsford, NY). The source transducer was normal to the specimen surface, and the receiving transducer was oriented at an oblique angle of $\theta_i = 24^{\circ}$ relative to the specimen surface. The normal incidence transducer transmitted a longitudinal wave into the sample, and the oblique incident receiveed scattered transverse energy. The water path (z_{fS}) was 20 mm for the longitudinal

transducer, and the material path was given by $z_S = \left(F - z_{fS}\right)c_f / c_L$. The number of waveform averages and the sampling frequency for the digitizer were 30 and 500 MHz, respectively. A total of 1,024 waveforms were collected by scanning the specimen over a rectangular grid of 8 mm × 8 mm. The spatial variance of all the waveform signals is shown in Figure 13.

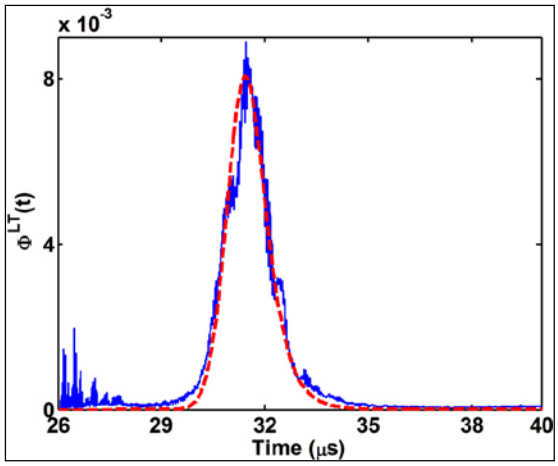

Figure 13. Experimental Variance Curve for the Type 1040 Alloy Steel Block Acquired from a 10-MHz Pitch-Catch Transducer Configuration Using the Fitted Theoretical LT Model

$L_{LT} = 16.9\ \mu$m was used to generate the fitted curve (dashed line) for the experimental variance curve (solid line).

The SSR measurement reveals the scattering from the microstructure of a specimen that can be observed in the portion of the signal between the front wall and back wall reflections. The theoretical LT model was used to fit the experimental result accordingly. As stated above, the only unknown in Equation (24) is the correlation length of the material as defined within the spatial correlation function $\tilde{\eta}_{LT}\left(\pi - \Theta\right)$, given by Equation (27). Inverting the experimental response $\Phi_{\exp}\left(t\right)$ by the theoretical L-T model without $\tilde{\eta}_{LT}\left(\pi - \Theta\right)$, the mean grain size L can be found (Ghoshal and Turner, 2010). For this operation, $\Lambda_1 = \Phi_{\exp}\left(t\right)$ and $\Lambda_2 = \Phi^{LT}\left(t\right) / \tilde{\eta}_{LT}\left(\pi - \Theta\right)$ are defined. Then, with Equation (27), an expression that depends only on L is identified from this ratio as:

$$\frac{\Lambda_1}{\Lambda_2} = \frac{L^3}{\pi^2\left[1 + L^2\left(k_L^2 + k_T^2 + 2k_L k_T \cos\Theta\right)\right]^2}. \tag{29}$$

A solution of this equation requires values for attenuations α_L and α_T within Λ_2. Because the attenuation from scattering is also dependent on correlation length (Weaver, 1990), an iterative approach is used here. An initial guess for L is made so that the attenuations can be estimated theoretically (Weaver, 1990). These values are then used in Λ_2 for Equation (29). At this point, the only physically meaningful root for L among the four possibilities is extracted from Equation (29). The correlation length is then used to update the attenuation estimates, and the

process is repeated until the value for L converges (usually after 5 to 6 iterations). For the sample examined here, this value was determined to be $L_{LT} = 16.9 \pm 0.1\ \mu\text{m}$.

The error in the measurement is the standard deviation from the average correlation length found from the inversion. The experimental spatial variance curve is compared with the theoretical result using L in Figure 13. The theoretical LT SSR model shows very good agreement with the experimental result. Furthermore, the difference between the mean correlation length of $L_{LT} = 16.9\ \mu\text{m}$ obtained from theoretical LT model and the grain size determined from optical microscopy, $L_{\text{opt}} = 17.8\ \mu\text{m}$, is 5%.

It is also important to compare the value of the correlation length from the LT approach with the value obtained from the more traditional LL pulse-echo type scattering measurements. Following a similar procedure, the mean correlation length extracted from the LL approach is $L_{LL} = 16.4 \pm 0.1\ \mu\text{m}$. The experimental result and the theoretical LL model with the mean correlation length of $L_{LL} = 16.4\ \mu\text{m}$ are shown in Figure 14. The theoretical LL model fits well at the early times and near the peak but deviates away from the experimental response a few microseconds after the focus. This deviation might be due to multiple scattering, but it is still under investigation. Clearly, the LT model fits the experimental measurement very well over the entire pulse width, suggesting that the single Gaussian beam assumed in the model is reasonable even when oblique incidence is used. It is also important to note that there is a much smaller material front wall reflection in the LT experiment, which is a significant advantage over the LL measurement, where scattering peaks often are easily affected by the front wall reflection unless sufficiently large material paths are used.

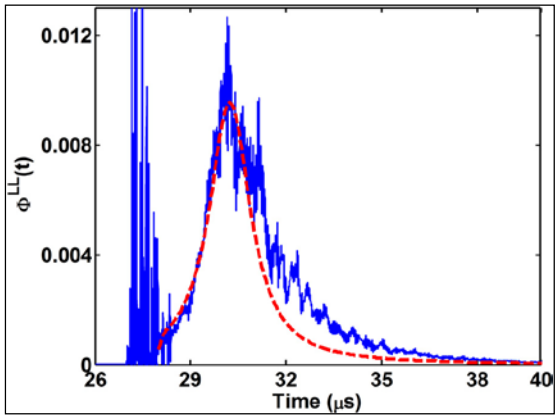

Figure 14. Experimental Variance Curve for the Type 1040 Alloy Steel Block Acquired from a 10-MHz Pulse-Echo Transducer Configuration Using the Fitted Theoretical LL Model

$L_{LT} = 16.4\ \mu\text{m}$ was used to generate the fitted curve (dashed line) for the experimental variance curve (solid line).

2.3 Summary

In this section, the theoretical basis of the grain scattering was derived with respect to the complete measurement system, including the transducer parameters, the focal depth in the material, and the properties of the polycrystalline medium. The dependence on the frequency

relative to the grain size was a critical factor for the measurements, because sufficient scattering was needed for the measurements, but the attenuation of the beam that penetrates the sample cannot be too high. The theory was developed for cases involving a single transducer used in a pulse-echo configuration as well as two transducers used in a pitch-catch configuration, one normally incident and one obliquely incident. The experimental results show the ability of the model to match the experiments, and the extraction of the material correlation length (related to the grain size) was demonstrated. In the next section, the influence of stress on the grain scattering is examined theoretically.

3. Polycrystalline Metals under Applied Stress

3.1 Theoretical Model

Acoustoelasticity refers to the study of the relationship between applied stress and wave speed within solids. This relationship results from higher-order material behavior, which can be neglected when linear-elastic approximations are sufficient for given applications. However, when strains are sufficiently large, the nonlinear behavior is a necessary and important aspect of the component or device response. Acoustoelastic behavior is typically examined in two forms.

First, the nonlinear response of single crystals is an important aspect of crystal resonators that undergo large accelerations or applied pressures due to the shifts in the resonant frequencies that result (Yang and Hu, 2004; Sinha and Tanski, 1985). Second, the acoustoelastic response of complex solids is often examined at a macro-scale level (Payan et al., 2009). Applications involving these materials are typically focused on monitoring stress in materials using ultrasonic methods (Santos and Bray, 2000; Kim and Hong, 2009).

Bridging these two scales has been successful only for polycrystals, for which single-crystal nonlinear behavior has been used to predict the nonlinear behavior of an ensemble of randomly oriented crystals (Ballabh et al., 1992; Powell and Skove, 1984). When the influence of applied stress on wave speeds is the sole interest, the models may rely on the first-order grain statistics alone for such predictions. This work has been very successful at connecting the different material scales. In the last several decades, higher-order spatial statistics of polycrystals have been of interest. The second-order grain statistics, through the covariance of the elastic moduli fluctuations, have been used to connect single crystal properties to ultrasonic scattering behavior that results when high-frequency waves pass through polycrystals. The impedance mismatch due to the misalignment of crystal axes causes energy to be lost from the primary propagation direction, an energy-conserving process. This scattering is most often quantified in terms of the attenuation or diffuse backscatter coefficient (Margetan et al., 1991; Ghoshal et al., 2007; Thompson et al., 2008; Stanke and Kino, 1984; Weaver, 1990; Lobkis and Rokhlin, 2010), as discussed in Section 2. The purpose of this section is to quantify the dependence of the second-order grain statistics on applied stress.

For unstressed materials, the first-order Voigt-average moduli are often defined as $\langle C_{ijkl}(x) \rangle$, where the angle brackets $\langle\ \rangle$ denote the ensemble average moduli. In most applications, an ergodic hypothesis is assumed such that the ensemble average may be replaced by a spatial average. For the second-order statistics, the quantity of interest $\langle C_{ijkl}(x) C_{\alpha\beta\gamma\delta}(y) \rangle$, involves two-point statistics. Simplification is often made through two assumptions. First, the material is assumed to be spatially homogeneous, such that the quantity of interest depends only on the difference between positions **x** and **y**. Second, and more importantly, for the model described in Section 3, the tensorial nature was assumed to be independent of the spatial nature. In this case, we write $\langle C_{ijkl}(x) C_{\alpha\beta\gamma\delta}(y) \rangle = \langle C_{ijkl} C_{\alpha\beta\gamma\delta} \rangle W(x-y)$, where the quantity W is a dimensionless function that contains all spatial dependence. The average, $\langle C_{ijkl} C_{\alpha\beta\gamma\delta} \rangle$, is therefore an angular average over all possible crystal orientations. It is the dependence of this quantity on applied stress that is of interest here. Thus, it is implicitly assumed that the applied stresses cause no geometric changes to the crystals.

The ultrasonic backscatter model described in Section 3 contains a covariance tensor, $\Xi = \left\langle C_{ijkl} C_{\alpha\beta\gamma\delta} \right\rangle - \left\langle C_{ijkl} \right\rangle \left\langle C_{\alpha\beta\gamma\delta} \right\rangle$ (Weaver, 1990; Ghoshal et al., 2007; Ghoshal and Turner, 2010). The covariance tensor influences the strength of the scattering that results from the reflections from inhomogeneous material grains. The stress dependency of the covariance can be formed when considering the second- and third-order single-crystal effective elastic moduli (Sorokin et al., 1994), defined as:

$$G_{ijkl} = C_{ijkl} + \left(\delta_{jl}\delta_{kP}\delta_{iQ} + 2C_{ijkr}S_{lrPQ} + C_{ijklmn}S_{mnPQ}\right)T_{PQ}, \tag{30}$$

where T_{pq} is the stress tensor, C_{ijkmnl} is the sixth-rank tensor of the third-order elastic moduli, C_{ijkl} is the second-order elastic moduli tensor, and $S_{ijkl} = C_{ijkl}^{-1}$.

The general form of Equation (30) is simplified by assuming that the material of interest contains a cubic symmetry. Under this assumption, the second-order elastic moduli can be written as:

$$C_{ijkl} = C_{ijkl}^{I} + \delta C_{ijkl} = C_{ijkl}^{I} + v\delta_{ijkl} = C_{ijkl}^{I} + v\sum_{n=1}^{3} a_{in}a_{jn}a_{kn}a_{ln} \tag{31}$$

where $v = C_{11}\text{-}C_{12}\text{-}2C_{44}$ is the single-crystal anisotropy coefficient for cubic materials, $C_{ijkl}^{I} = C_{12}\delta_{ij}\delta_{kl} + C_{44}\left(\delta_{ik}\delta_{jl} + \delta_{il}\delta_{jk}\right)$, and a_{ij} is a rotation matrix containing Euler angles $\Phi, \theta,$ and ζ that define the crystal orientation relative to generalized coordinates. The third-order elastic moduli were derived by Ballabh et al. (1992) for materials containing cubic symmetry as:

$$C_{ijklmn} = C_{123}\delta^{1}_{ijklmn} + C_{144}\delta^{2}_{ijklmn} + C_{456}\delta^{3}_{ijklmn} + d_1 A^{[1]}_{ijklmn} + d_2 A^{[2]}_{ijklmn} + d_3 A^{[3]}_{ijklmn} \tag{32}$$

where only six third-order elastic constants are important (Ballabh et al., 1992). The anisotropy constants $d_{1\text{-}3}$ are:

$$\begin{aligned} d_1 &= C_{111} - 3C_{112} + 2C_{123} + 12C_{144} - 12C_{166} + 16C_{456}\ , \\ d_2 &= C_{112} + C_{123} - 2C_{144}\ , \text{ and} \\ d_3 &= C_{166} - C_{144} - 2C_{456} \end{aligned} \tag{33}$$

The isotropic base tensors are given by:

$$\begin{aligned} I_{ijkl} &= \frac{1}{2}\left(\delta_{ik}\delta_{jl} + \delta_{il}\delta_{jk}\right), \\ \delta^{1}_{ijklmn} &= \delta_{ij}\delta_{kl}\delta_{mn}, \\ \delta^{2}_{ijklmn} &= 2\left(\delta_{ij}I_{klmn} + \delta_{kl}I_{ijmn} + \delta_{mn}I_{ijkl}\right), \text{ and} \\ \delta^{3}_{ijklmn} &= 2\left(\delta_{ik}I_{jlmn} + \delta_{il}I_{jkmn} + \delta_{im}I_{jnkl} + \delta_{in}I_{jmkl}\right)\ . \end{aligned} \tag{34}$$

The tensors A^1, A^2, and A^3 are written in terms of the rotation matrix:

$$
\begin{aligned}
A^{[1]}_{ijklmn} &= a_{iu}a_{ju}a_{ku}a_{lu}a_{mu}a_{nu}, \\
A^{[2]}_{ijklmn} &= \delta_{ij}a_{ku}a_{lu}a_{mu}a_{nu} + \delta_{kl}a_{iu}a_{ju}a_{mu}a_{nu} + \delta_{mn}a_{iu}a_{ju}a_{ku}a_{lu}, \\
A^{[3]}_{ijklmn} &= \delta_{ik}a_{ju}a_{lu}a_{mu}a_{nu} + \delta_{il}a_{ku}a_{ju}a_{mu}a_{nu} + \delta_{im}a_{ju}a_{ku}a_{lu}a_{nu} + \delta_{in}a_{ju}a_{ku}a_{lu}a_{mu} \\
&\quad + \delta_{jk}a_{iu}a_{lu}a_{mu}a_{nu} + \delta_{jl}a_{iu}a_{ku}a_{mu}a_{nu} + \delta_{jm}a_{iu}a_{ku}a_{lu}a_{nu} + \delta_{jn}a_{iu}a_{ku}a_{lu}a_{mu} \\
&\quad + \delta_{km}a_{iu}a_{ju}a_{lu}a_{nu} + \delta_{kn}a_{iu}a_{ju}a_{lu}a_{mu} + \delta_{lm}a_{iu}a_{ju}a_{ku}a_{nu} + \delta_{ln}a_{iu}a_{ju}a_{ku}a_{mu}
\end{aligned}
\tag{35}
$$

where the components are summed over index u.

The average effective elastic moduli can now be written as:

$$
\left\langle G_{ijkl} \right\rangle = \left\langle C_{ijkl} \right\rangle + \left(\delta_{jl}\delta_{kP}\delta_{iQ} + 2\left\langle C_{ijkr}S_{lrPQ} \right\rangle + \left\langle C_{ijklmn}S_{mnPQ} \right\rangle \right) T_{PQ}, \tag{36}
$$

where C_{ijkl} are the averaged unstressed moduli. After much simplification, the general form of the covariance tensor is found:

$$
\begin{aligned}
\Xi^{\alpha\beta\gamma\delta}_{ijkl}(T) = \left\langle G_{ijkl}G_{\alpha\beta\gamma\delta} \right\rangle - \left\langle G_{ijkl} \right\rangle \left\langle G_{\alpha\beta\gamma\delta} \right\rangle &= \left\langle C_{ijkl}C_{\alpha\beta\gamma\delta} \right\rangle - \left\langle C_{ijkl} \right\rangle \left\langle C_{\alpha\beta\gamma\delta} \right\rangle \\
&\quad + 2\left(\left\langle C_{ijkr}S_{lrPQ}C_{\alpha\beta\gamma\delta} \right\rangle - \left\langle C_{ijkr}S_{lrPQ} \right\rangle \left\langle C_{\alpha\beta\gamma\delta} \right\rangle \right) T_{PQ} \\
&\quad + 2\left(\left\langle C_{ijkl}C_{\alpha\beta\gamma\rho}S_{\delta\rho RT} \right\rangle - \left\langle C_{ijkl} \right\rangle \left\langle C_{\alpha\beta\gamma\rho}S_{\delta\rho RT} \right\rangle \right) T_{RT} \\
&\quad + 4\left(\left\langle C_{ijkr}S_{lrPQ}C_{\alpha\beta\gamma\rho}S_{\delta\rho RT} \right\rangle - \left\langle C_{ijkr}S_{lrPQ} \right\rangle \left\langle C_{\alpha\beta\gamma\rho}S_{\delta\rho RT} \right\rangle \right) T_{RT}T_{PQ} \\
&\quad + \left(\left\langle C_{ijklmn}S_{mnPQ}C_{\alpha\beta\gamma\delta} \right\rangle - \left\langle C_{ijklmn}S_{mnPQ} \right\rangle \left\langle C_{\alpha\beta\gamma\delta} \right\rangle \right) T_{PQ} \\
&\quad + 2\left(\left\langle C_{ijklmn}S_{mnPQ}C_{\alpha\beta\gamma\rho}S_{\delta\rho RT} \right\rangle - \left\langle C_{ijklmn}S_{mnPQ} \right\rangle \left\langle C_{\alpha\beta\gamma\rho}S_{\delta\rho RT} \right\rangle \right) T_{RT}T_{PQ} \\
&\quad + \left(\left\langle C_{ijkl}C_{\alpha\beta\rho\delta\sigma\lambda}S_{\sigma\lambda RT} \right\rangle - \left\langle C_{ijkl} \right\rangle \left\langle C_{\alpha\beta\gamma\delta\sigma\lambda}S_{\sigma\lambda RT} \right\rangle \right) T_{RT} \\
&\quad + 2\left(\left\langle C_{ijkr}S_{lrPQ}C_{\alpha\beta\gamma\delta\sigma\lambda}S_{\sigma\lambda RT} \right\rangle - \left\langle C_{ijkr}S_{lrPQ} \right\rangle \left\langle C_{\alpha\beta\gamma\delta\sigma\lambda}S_{\sigma\lambda RT} \right\rangle \right) T_{RT}T_{PQ} \\
&\quad + \left(\left\langle C_{ijklmn}S_{mnPQ}C_{\alpha\beta\gamma\delta\sigma\lambda}S_{\sigma\lambda RT} \right\rangle - \left\langle C_{ijklmn}S_{mnPQ} \right\rangle \left\langle C_{\alpha\beta\gamma\delta\sigma\lambda}S_{\sigma\lambda RT} \right\rangle \right) T_{RT}T_{PQ}.
\end{aligned}
\tag{37}
$$

The covariance tensor is now in a form that is quadratic in the applied stress, with coefficients containing second- and third-order elastic constants. The covariance is reduced considerably because only nine elastic constants remain after considering the single-crystal symmetry. Furthermore, Equation (37) can be written in a condensed form in terms of the magnitude of applied stress, as:

$$
\Xi^{\alpha\beta\gamma\delta}_{ijkl} = K_0 + K_1 T + K_2 T^2 \tag{38}
$$

where the constants K_j are defined as stress-dependent backscatter coefficients. The second- and third-order constants needed to calculate the backscatter coefficients are given in Table 1. The backscatter coefficients for shear-mode scattering are given in Table 2.

Table 1. Second- and Third-Order Elastic Constants Used to Calculate Backscatter Coefficients

Material	C_{11}	C_{12}	C_{44}	C_{111}	C_{112}	C_{123}	C_{144}	C_{166}	C_{456}
Fe	229.3	134.1	116.7	-2,720	-608	-578	-836	-530	-720
Al	107.0	61.0	28.0	-1,080	-315	36	-23	-340	-30
MgO	397.1	95.4	156.1	-4,895	-95	-69	113	-659	147
Au	192.9	163.8	41.5	-1,729	-922	-233	-13	-648	-12

Sources: (Powell and Skove, 1984; Ballabh et al., 1992)

Table 2. Backscatter Coefficients Used to Calculate the Stress-Dependent Covariance Modulus for Uniaxial Loading (Turner and Ghoshal, 2010)

Material	Ξ_{1313}^{1313}			Ξ_{2323}^{2323}		
	K_0 (GPa^2)	K_1 (GPa)	K_2	K_0 (GPa^2)	K_1 (GPa)	K_2
Fe	327.4	-39.02	16.17	327.4	56.37	6.458
Al	1.714	1.312	9.287	1.714	-1.715	6.218
MgO	209.3	33.61	3.520	209.3	-39.91	2.516
Au	49.80	-8.950	26.05	49.80	8.707	9.514

Source: (Turner and Ghoshal, 2010)

3.2 Example Results for Uniaxial Stress

To compute the covariance computationally, only nine terms are needed due to the symmetry of several terms. The covariance clearly varies quadratically with applied stress as shown by Equation 38. The coefficient K_0 is the covariance of the elastic moduli for the unstressed material (as described in Section 2), which has been examined by several others previously (Margetan et al., 1991; Weaver, 1990; Thompson et al., 2008; Lobkis and Rokhlin, 2010; Ghoshal et al., 2007; Ghoshal and Turner, 2010) and is described in Section 2 above. The stress-dependent components, encompassed by K_1 and K_2, have not been examined before.

Example results are presented below for uniaxial loading—a specific case of importance in longitudinal rail stress and in other applications. We assume that an initially stress-free material is loaded uniaxially along the 1-direction, such that the four subscripts in Equation (37) are given: $R = T = P = Q = 1$. We also restrict the results to four specific cases. The quantities $\Xi_{2222}^{2222} = \Xi_{3333}^{3333}$ are related to normal incidence ultrasonic backscatter experiments in a direction perpendicular to the applied uniaxial load, and Ξ_{1111}^{1111} is related to such experiments in the direction parallel to the applied load. Finally, two other components, Ξ_{1313}^{1313} and Ξ_{2323}^{2323}, are important because they are associated with shear-wave scattering.

A comparison between the first-order and second-order responses of aluminum to an applied unaxial load is shown in Figure 15. In these plots, the range of stress values encompasses approximately the yield strength. Also, all plots in both graphs are normalized to the zero stress state so that the relative change in these values can be observed (for the unnormalized values we multiply by K_0). We see that the first-order response (change in wave speed) in the left panel of Figure 15 varies by more than 10% over this stress range. In contrast, in the right panel, the

second-order response varies by more than 100% for all cases. In particular, the longitudinal scattering is significantly higher in the direction parallel with the applied stress.

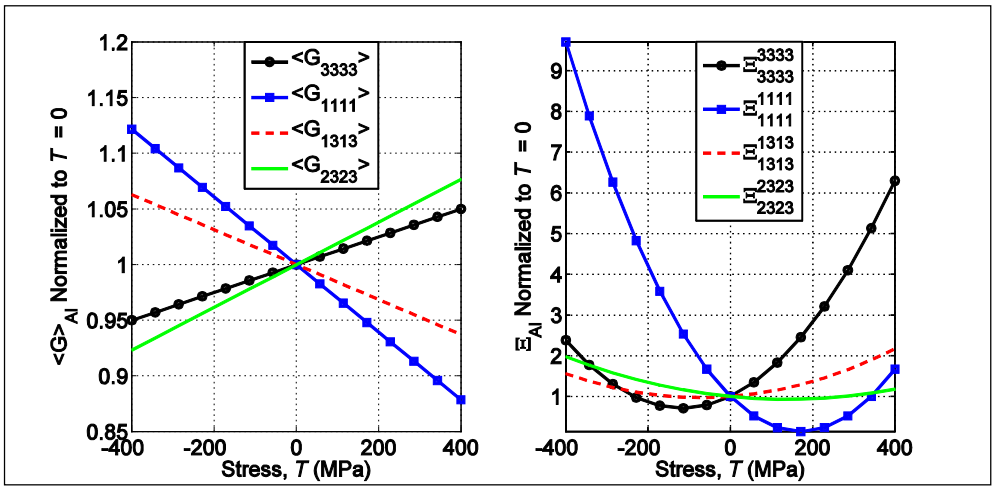

Figure 15. Example Results for Polycrystal Aluminum Subject to a Uniaxial Stress Applied in the 1-Direction

Left: First-order response that governs the wave speeds for different components [Equation (34)]. **Right:** Second-order response that governs ultrasonic scattering for different components [Equations (35) and (36)].

The different curves in Figure 16 represent the longitudinal wave mode, Ξ^{3333}_{3333}, and the two shear wave modes (orthogonal), Ξ^{1313}_{1313} and Ξ^{2323}_{2323} (Turner and Ghoshal, 2010). The independent stress responses seen in the different curves can be advantageous for practical stress measurements. The measurement of stress through one transducer can be confirmed or averaged by measurements from the other transducers. This result can ultimately lead to more precise measurements of the stress state. The other utility comes through observing the intersection of the curves at the location of zero stress. Thus, the measurement of stresses from multiple transducers can allow for extrapolation back to the location of zero stress. This process could result in a method for calculating the rail neutral temperature (RNT) in CWR.

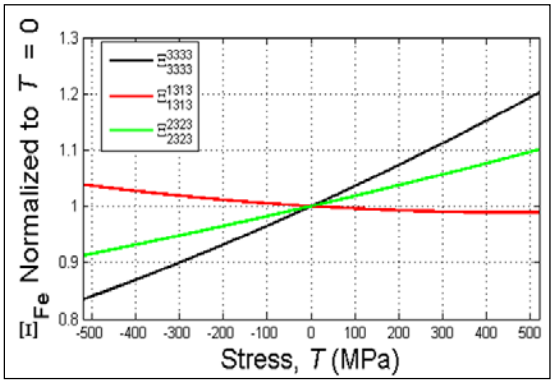

Figure 16. Theoretical Covariance Curves for Longitudinal (Ξ^{3333}_{3333}) and Shear (Ξ^{1313}_{1313} and Ξ^{2323}_{2323}) Modes in Iron

3.3 Summary

The theoretical basis for the expected changes in the diffuse ultrasonic backscatter with stress was described in this section. It was shown that the different scattering modes (e.g., LL, and longitudinal-to-shear) had very different trends, especially when their behavior was in relation to the applied stress direction. Thermally generated stress in rail was dominated by the component along the axis of the track, and it was often considered to be uniaxial. Thus, the expected changes in diffuse ultrasonic backscatter for the different scattering modes have the potential to be used to measure and monitor longitudinal rail stress. The approach to the experimental aspects of this project are described next in Section 4.

4. Stress Monitoring with Ultrasonic Backscatter

In Sections 2 and 3, the theoretical basis for the stress dependency contained within the elastic contribution to scattering of ultrasonic waves was described. A stress-dependent covariance tensor defined the mean point-to-point spatial fluctuations of the local elastic tensor. In this section, two experimental techniques, motivated by the stress-dependent grain statistics, are developed and explored. The experimental techniques are considered within both a laboratory setting and a field setting, with comparisons made between thermally generated stresses and scattering measurements. Emphasis is placed on the development of techniques for thermal stress measurement for railroad applications, although it is clear that there are other potential applications this work as well.

4.1 Diffuse Ultrasonic Backscatter Methods

The covariance tensors defined in Sections 2 and 3 quantify the mean fluctuation of point-to-point elastic moduli tensors caused by a non-zero stress state. In order to take advantage of the stress-dependency of the covariance tensors (Section 3), experimental methods should be constructed as such so that the stress-dependent covariance directly impacts the measured quantities. Such experiments are often referred to as *diffuse scattering measurements* or *diffuse field measurements*. The following subsections outline two different experimental configurations and signal processing techniques used to achieve diffuse measurements on rail in various stress states both in the laboratory and in the field.

4.1.1 Spatial Variance Method

As outlined in Section 2, ultrasonic backscatter results from the interactions between ultrasound and the grain microstructure in polycrystalline materials. The interface boundaries between adjoining grains contain acoustic impedance mismatches which result in scattered reflections. These reflections are observed through receiving transducers such that information about the microstructure can be inferred.

The scattering has been quantified in terms of attenuation models and a diffuse backscatter coefficient (Margetan et al., 1991; Thompson et al., 2008; Lobkis and Rokhlin, 2010; Ghoshal et al., 2007; Ghoshal and Turner, 2010). These models have been successfully applied to extract microstructural parameters such as grain size, grain texture, microcracks, and inclusions. One model used to extract grain size was developed by Ghoshal and Turner (2010) for a normally incident transducer and was later expanded to a pitch-catch oblique incidence configuration for mode conversion (Hu et al., 2013). It predicts the grain size by using a correlation length parameter determined through the spatial variance of a collection of scattered signals. The model also depends on the covariance tensor defined in Sections 2 and 3. Here, the theoretical model is compared to experiments by considering spatial averaging techniques in order to quantify the diffuse scattering properties. This result is achieved by scanning a material at different locations while acquiring the scattered signals. Focused transducers are often used in order to direct more ultrasonic energy on axis, which results in an increase of the scattered response. This process is shown for a normally incident focused transducer in Figure 17.

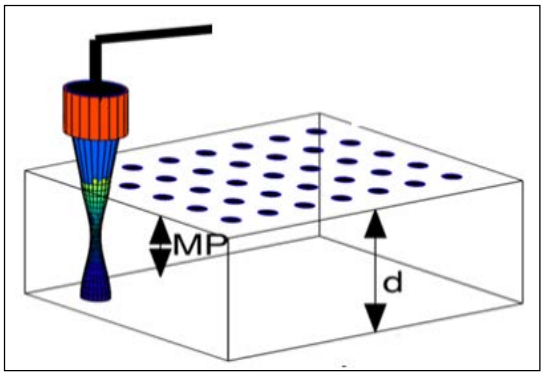

Figure 17. Ultrasonic Scanning Performed Over a Sample to Determine Measured Spatial Variance Proportional to the Diffuse Backscatter Coefficient

The spatial variance is then found by

$$\Phi(t) = \langle V(t)^2 \rangle - \langle V(t) \rangle^2, \tag{39}$$

where $\langle V(t) \rangle$ is the amplitude average of a matrix $V(t)$ containing the scattered signals as a function of time. The spatial variance for a 10-MHz focused transducer from an experiment performed on a steel sample is shown in Figure 18.

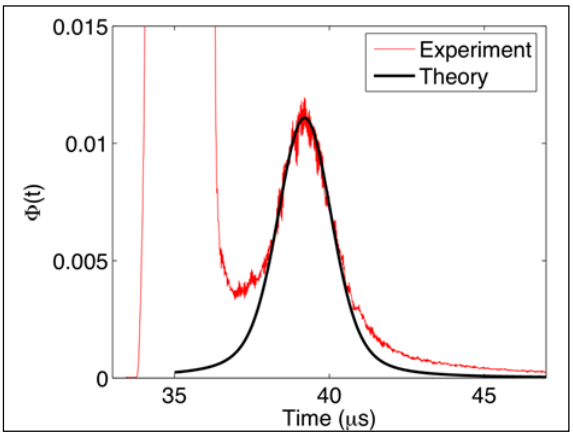

Figure 18. Single Scattering Response from a Sample of Steel

The first part of the variance is the reflection from the surface of the material or the frontwall. The scattering occurs in the region just beyond the frontwall and is easily recognized by its Gaussian shape. The response contained near the peak of the experimental variance is commonly referred to as the SSR, because the returned ultrasonic energy within this region is assumed to have been scattered only once while within the material. The theoretical model of the SSR response, as described in Section 2, is represented by the black curve in Figure 18.

The SSR proves to be sensitive to the microstructure, and slight microstructure fluctuations can be observed within the model. This concept has led to the idea of relating the SSR to externally applied loads, which will cause slight variations in grain elasticity. This relationship was formally derived by Turner and Ghoshal (2010) through the use of second-order grain statistics and, specifically, the covariance of elastic moduli as described in Section 3. The derivation of the

load-dependent covariance tensor, $\Xi_{ijkl}^{\alpha\beta\gamma\delta}$, formed the basis for the stress measurement approach described here.

4.1.2 Single-Point Autocorrelation Method

Often, the ability to scan a material spatially is not feasible due to geometrical constraints or poor ultrasonic coupling. In such cases, stress measurements using a stationary, single-point technique are desired. This result can be achieved by averaging over scattering events through the depth of the material rather than spatial averaging accomplished through scanning. The resulting single-point scattered waveform is shown in Figure 19.

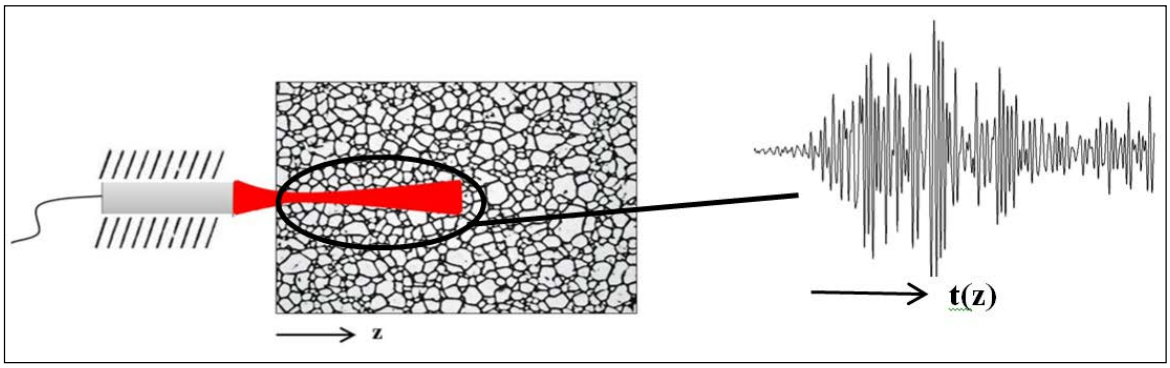

Figure 19. Single-Point Ultrasonic Insonification Over Grains Along the Depth Direction, and the Resulting Scattered Waveform

Averaging the scattering events along the depth dimension z or equivalently in time t, through wave velocity relations, is done through the use of the discrete autocorrelation function for a strongly stationary process:

$$(\tau) = E[\phi_t \phi_{t-\tau}] \quad , \tag{40}$$

where E is the expectation operator. The autocorrelation function is numerically related to the spatial variance through the use of the Weiner-Khinchin theorem (Carrier et al., 1983):

$$\sqrt{\int R_{\phi\phi} dt} \approx \langle \phi_T^2(t) \rangle. \tag{41}$$

This result gives a single-point approximation of the covariance tensor components along with the associated stress dependences described in Section 3.

Single-point backscatter measurements using Equation (41) require the autocorrelation function to be calculated over a gated or windowed region of a scattered signal. A scattered waveform obtained from oblique incidence (shear mode) configuration and an example of a windowed region are shown in Figure 20.

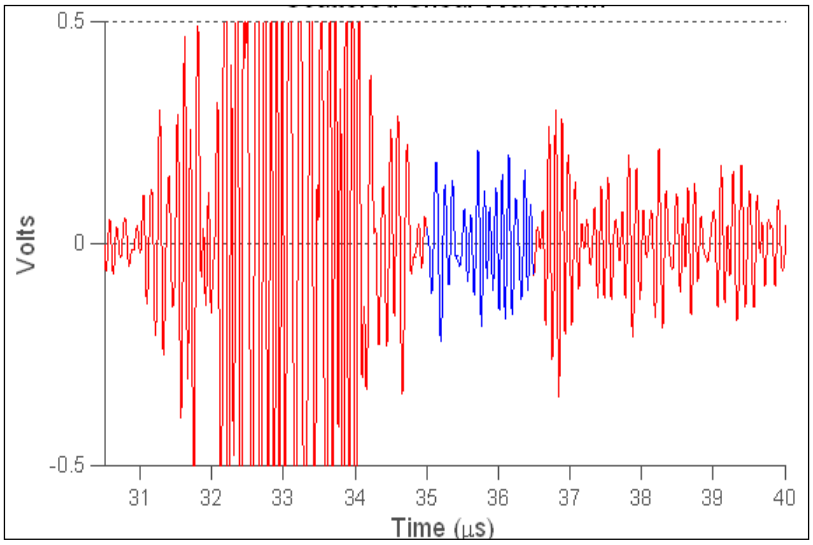

Figure 20. Ultrasonic Waveform Displaying Grain Scattering for an LT Scattering Configuration

The blue gated region is an example of a region to perform the autocorrelation for a backscatter measurement.

The blue region of the signal is a typical scattering window used in a backscatter measurement. During experiments, the autocorrelation [Equation (41)] is numerically applied to this region, and its amplitude can be related to the applied stress. The location and selection of the windowed region should correspond with the SSR described in Section 2.2 when comparing with the theoretical model. Selecting windows exceeding this region are also stress dependent but contain higher-order multiplying or fully diffuse scattering effects. The ideal window parameters used for practical stress measurements have been explored preliminarily but are not yet determined. The window region used to obtain the single-point results in Sections 3.2-3.4 was centered near the peak of the SSR region, with a width of approximately 1.5 μs. The signal processing techniques used to perform the single-point backscatter calculation are described below.

4.2 Laboratory Experiments

In order to observe the backscatter/stress dependence in well-controlled conditions, several laboratory compression and tensile experiments were conducted on a variety of materials, including steel, aluminum, magnesium oxide, and rail steel. As shown in Section 3, the relation between the scattering strength and the stress is material dependent. In addition, the dependence of the scattering on the stress depends on the specific measurement configuration (i.e., pulse-echo, pitch-catch) relative to the loading direction. The use of various sample types and the two loading configurations allowed for a broad comparison with the theoretical model.

4.2.1 Laboratory Tensile Experiments

The first test fixture was designed and built in order to induce a uniaxial tensile stress into metallic samples while ultrasonic measurements could perform within a standard ultrasonic immersion tank. The model drawing is shown in Figure 21.

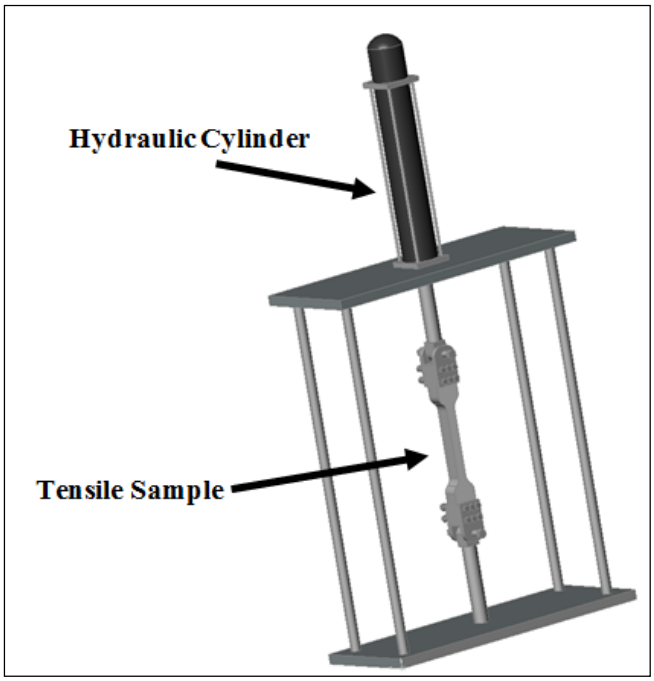

Figure 21. Model Drawing of the Tensile Fixture Designed to Apply Loads on Samples for Measurements of Spatial Variance as a Function of Applied Load

The fixture utilized a dual-acting hydraulic cylinder at its top to vertically load the dog-bone-shaped samples held between the ends. The samples were designed with this shape in order to produce near uniaxial stress at their midspan. The dimensions of the fixture allowed for easy placement into the scanning ultrasonic immersion tank (Figure 22). The immersion (water) tank is necessary to ensure adequate coupling so that the ultrasound is properly transmitted into the sample.

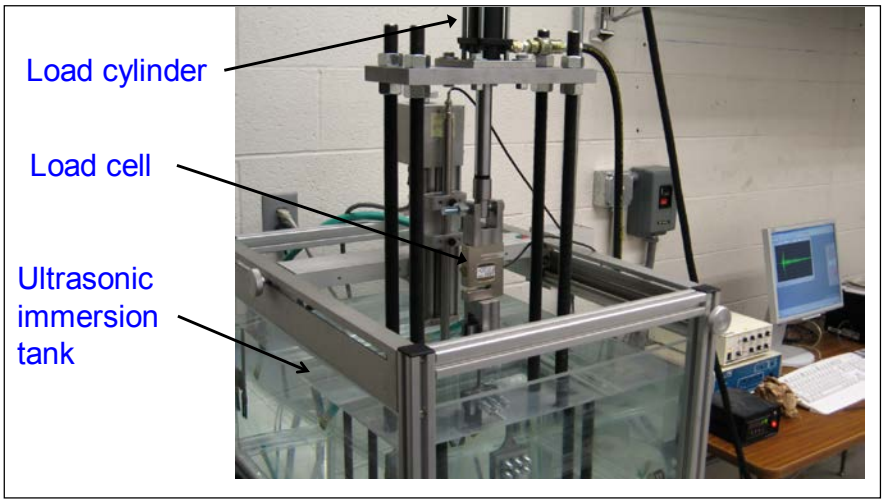

Figure 22. Photograph of the First Test Setup Used to Perform Ultrasonic Scans for the Calculation of the Spatial Variance as a Function of Stress

This setup allowed for a transducer to scan the surface of the tensile stressed sample while collecting scattered signals. The scanning was performed by a stepper motor controlled through a

connected computer and *UTWin* software. The software allows the selection of scanning speed and resolution (distance between consecutive collected signals). The resolution was chosen to be greater than one-half wavelength to ensure insonification of different grains at each location. The transducers were excited using a *JSR DPR-300* pulser/receiver. The waveforms were sampled through a 500-MHz digitizer card in the computer (a digitizer is a data acquisition device that converts the analog ultrasonic signals into digital waveforms).

Typical scans consisted of collecting 300 to 500 waveforms. Collecting fewer waveforms often resulted in irresolvable scattering peaks. The scans were performed at a number of different loads up to 5,000 lb. The loads were measured by the use of a load cell placed inline with the load cylinder and the tensile sample. After the scans were finished, the data were exported into *Matlab*, where signal alignment and variance calculation were performed.

This procedure was utilized to explore the relationship between the spatial variance and uniaxial loads for samples of magnesium oxide, aluminum alloy, and steel. For a number of possible reasons, the results of this testing produced many inconclusive results when compared to the predicted theoretical curves. Therefore, the results presented in this section do not encompass the large number of experiments performed using this procedure, but rather highlight the major important point that backscatter is highly dependent on the material stress state.

To illustrate the trends observed, a sample of a magnesium alloy was scanned at normal incidence using a 15-MHz focused transducer. The cross-section of the sample measured 10 mm x 10 mm. The scan consisted of collecting 350 waveforms at each of a number of different applied tensile loads. The variance was calculated. The single scattering peaks are shown in Figure 23.

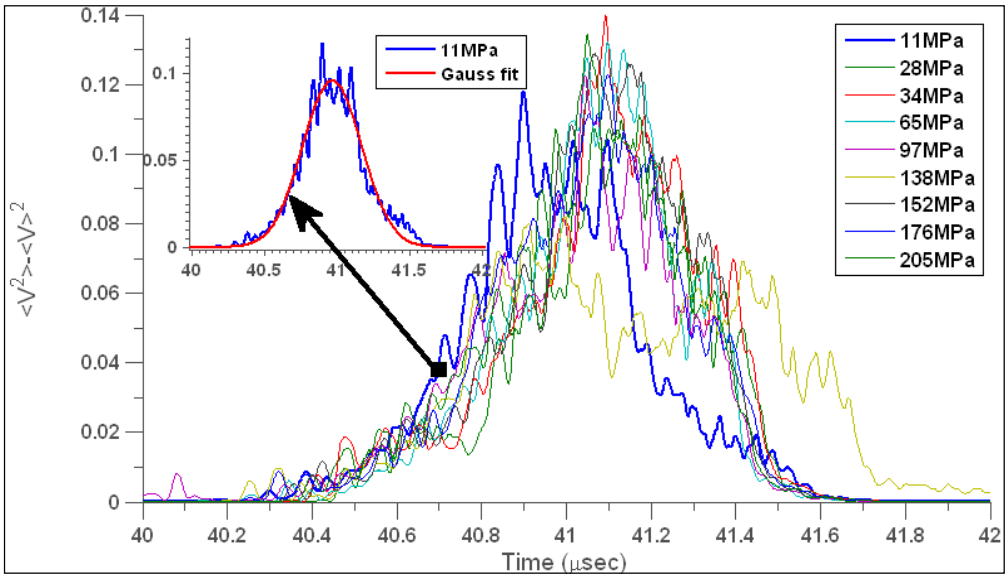

Figure 23. Single Scattering Peaks for Normal Incidence Ultrasound on a Magnesium Alloy as a Function of Stress

In order to quantify any differences among the peaks, a Gaussian curve was fit to each of the data sets. The single-term Gaussian fit took the following form:

$$\Phi(t) = Ae^{-\left[(t-b)/c\right]^2} \quad , \tag{42}$$

where *A, b,* and *c* were used as fitting parameters. An example curve fit is shown in the inset of Figure 23. Clearly, the Gaussian function is appropriate for the measurement data. The amplitude *A* that was determined during each of the fits was used for comparison with the applied stress. This result is shown in Figure 24, where the experimental amplitudes are represented by the green data points. The red line shown is a quadratic curve fit to the data.

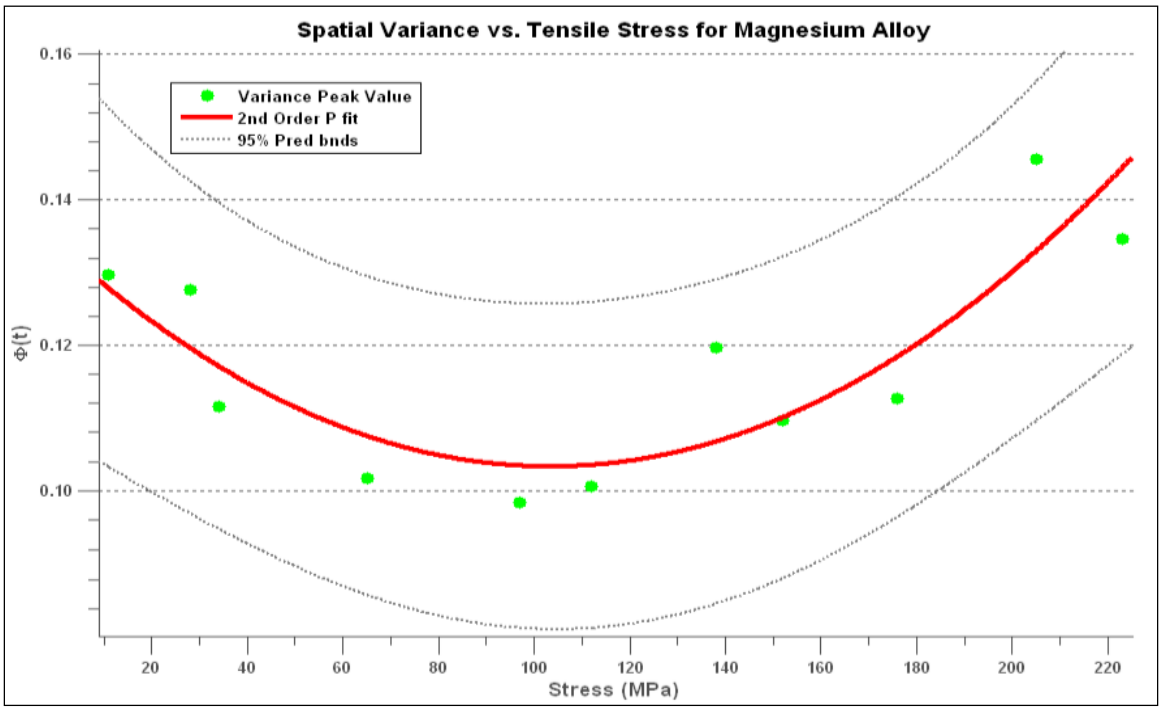

Figure 24. Peak Values of the Gaussian Fit to Single Scattering Peaks as a Function of Stress for a Magnesium Alloy

The second-order polynomial fit shows the quadratic relationship with the stress for the magnesium oxide sample. This result differs from the theoretical curve shown in Figure 25 for an assumed polycrystal of MgO. The theoretical curve shows a negatively sloped, linear stress dependence over the experimental stress range used. The deviation between the theoretical and experimental data could be attributed to a number of reasons.

The theoretical data are based on second- and third-order single-crystal elastic constants, which are obtained from work performed previously in which the constants for pure materials (i.e., non-alloyed metals and iron) were determined (Powell and Skove, 1984; Ballabh et al., 1992). Because the tensile samples used in these tests (magnesium oxide, aluminum alloy, and steel) were not pure forms, we have assumed the elastic constants of their nearest relations. In order to generate accurate theoretical curves, single-crystal constants of the tested samples should be measured; however, they were not performed in this case, because they would be costly, would need to be outsourced, and were deemed to be beyond the scope of this project.

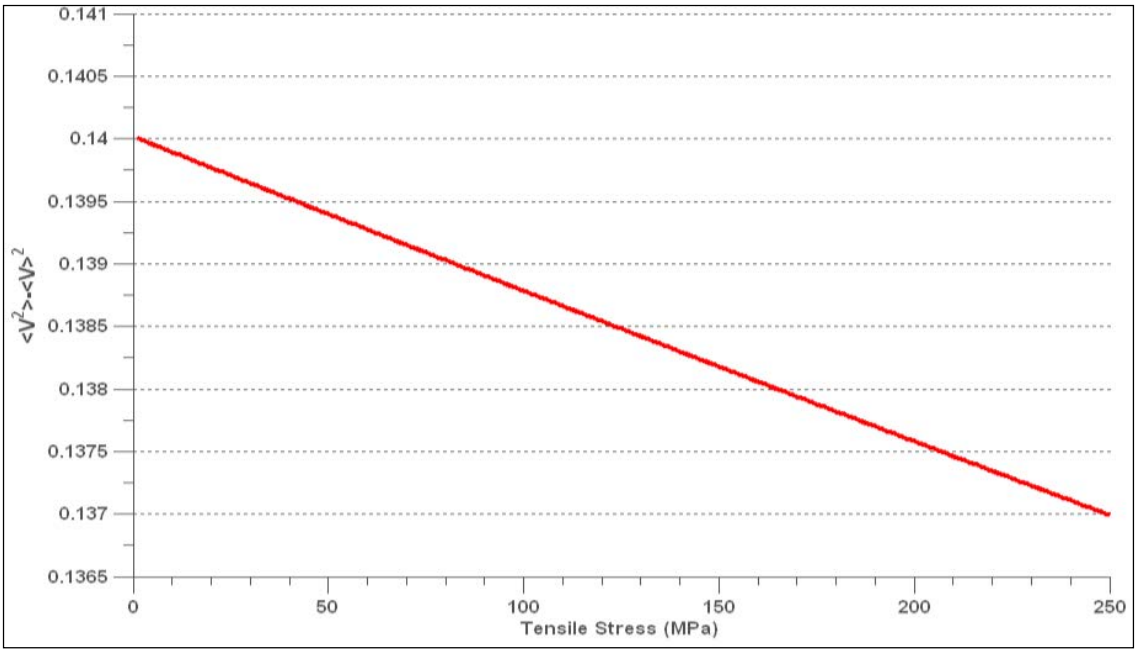

Figure 25. Theoretical SSR Amplitude as a Function of Applied Stress, Based on the Single-Crystal Elastic Constants of Magnesium Oxide

Experimental errors are also believed to exist within the loading fixture and the tensile samples. The loading fixture utilized a dual-acting, hydraulic cylinder to load and unload the samples. The application of a load or incrementing from a previous load was performed using an electronic switch that activated the solenoid within the hydraulic pump. This process caused the load to be applied suddenly to the sample, which often would cause the sample to jerk and rotate. The rotation affects the measurement results, because the angle between the sample and the transducer causes a drop in the signal amplitude, which could greatly impact the value of the spatial variance.

The relatively small dimensions of the sample (10 mm x 10 mm) also are a potential source of experimental error. A typical ultrasonic signal has a beam diameter of 2 to 3 mm. This broad beam diameter causes the transmitted ultrasound to be reflected inadvertently and scattered from the sides and corners of the sample. A drop in the scattered signal results when the scanning transducer approaches these locations.

These effects were evident when the loading experiments were performed. However, it was reasonable to assume that the change in the spatial variance with load was not due solely to these factors, based on the fact that the experiments produced repeatable and continuous backscatter/stress curves. Furthermore, the net change in the spatial variance over the loading range was greater than could be produced from the sources of error alone.

The results shown in Figure 25 were typical for other samples tested with this load fixture, including an aluminum alloy and a steel alloy. The observed stress dependence motivated further progression of this research. It was evident that measurements needed to be performed outside the scanning ultrasonic tank to eliminate the observed errors. In addition, these measurments provided insight into the challenges of measurements on in-service rail using an attached stationary device.

4.2.2 Laboratory Compression Experiments

An additional series of laboratory experiments were also designed for compressive loads. Because test specimens must be designed differently when tension and compression are concerned, a completely different load fixture was used. Initially, the goal was to measure the spatial variance using the same scanning methods described in Section 2. Thus, the experiment design involved an ultrasonic immersion tank that was built within the test frame of a 440,000-lb load fixture within the Civil Engineering test bay at the University of Nebraska-Lincoln (UNL). The immersion tank included the same 3-axis motion control such that the focal depth and scan area were controlled independently. A photograph of the experimental setup is shown in Figure 26. The transducer was mounted on a manually controlled gimbal in order for the incidence angle to be controlled precisely.

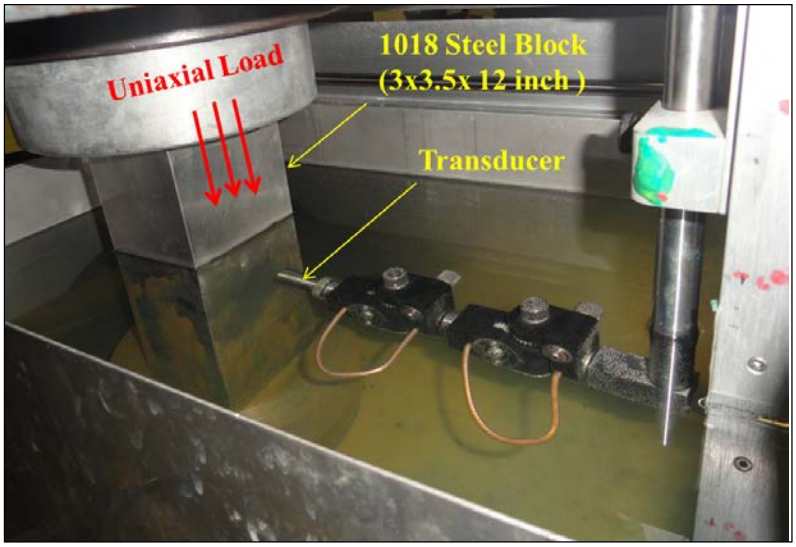

Figure 26. Photograph of the Experimental Setup for the Spatial Variance Measurements Under a Uniaxial Compressive Load

Experiments were conducted in a water immersion tank using a 10-MHz transducer (Panametrics V327-SU; 12.5-mm diameter; 50-mm focal depth) focused 8.5 mm into a block of annealed 1018 steel. Typical experiments were performed by acquiring wave-forms in a pulse-echo configuration for which the ultrasonic propagation direction was normal to the steel block but perpendicular to the loading direction. Figure 27 shows a schematic of the measurements with the geometry defined. The backscatter coefficient was evaluated by scanning a normal incidence transducer along the x-y plane, and an optical analysis was performed on the surface to determine the true grain size.

The scattered signals were obtained from the waveforms by observing the energy between the front and back surface reflections. The spatial variance was determined from the collection of scattered signals obtained at 1000 different locations (within a 10 cm x 10 cm area) while keeping a fixed distance between the transducer and the material. The stress-free experimental results and corresponding theoretical fit (0 MPa curves) are shown in Figure 28. The high amplitude portion of the measurement that occurs at an earlier time was due to the front wall reflection from the sample. Because high amplifier gains are necessary to observe the scattering from the microstructure, the front wall reflection was saturated.

The experimental SSR response was fit using Equation (9), for which the correlation length was used as the single-fit parameter (Ghoshal and Turner, 2010). It should be noted that the attenuation was relevant in the model for these experiments due to the strong scattering within the sample (0.04 Np/cm was used, based on theoretical and experimental estimates). This fit resulted in an estimated grain length of 34 μm, which was within 2.6% of the 33.1-μm grain length (mean distance between grain boundaries) obtained from optical microscopy (see the etched micrograph shown in Figure 27). In terms of the raw experimental data, the stress-free measurement also gave a peak value of $\Phi_{peak} = 8.5 \times 10^3$ V^2 for the experimental settings used.

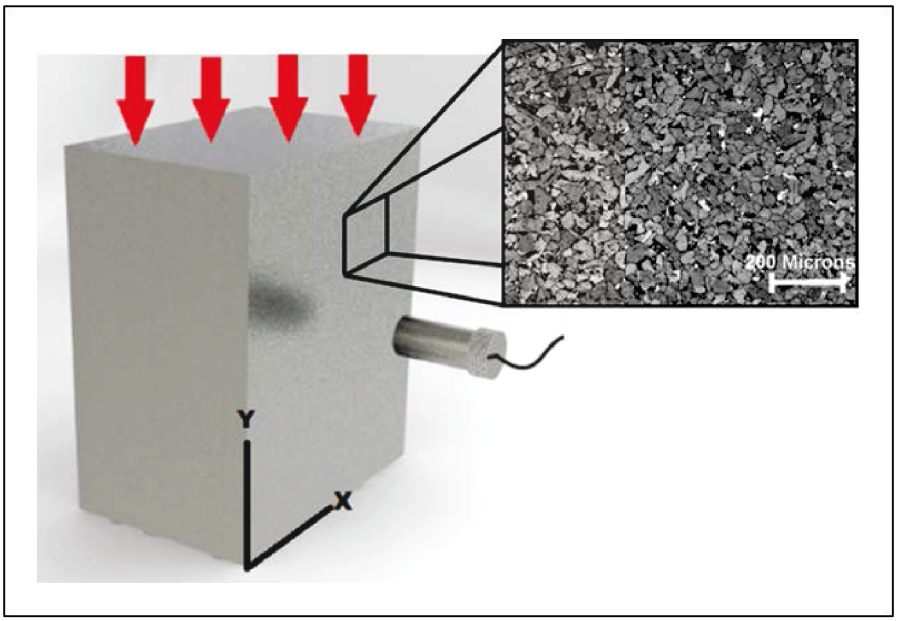

Figure 27. Schematic of Spatial Variance Measurements Geometry, with Etched Micrograph

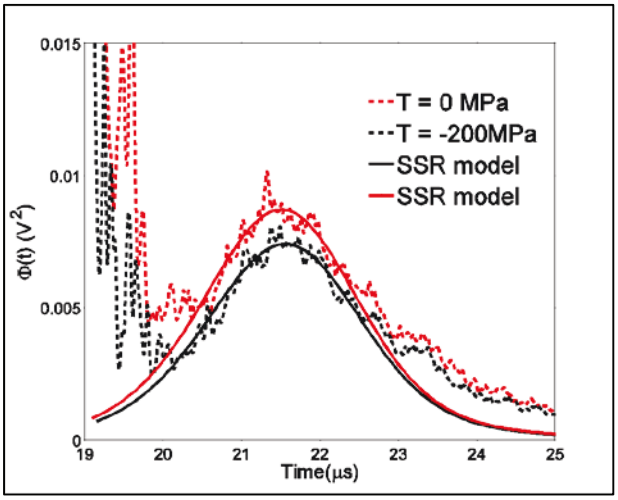

Figure 28. Experimental Results and Theoretical Fit Using a 10-MHz Focused Transducer on a Stress-Free Compressively Loaded 1080 Steel Sample

Next, the measurements under an applied load were considered. The peak value of the backscatter coefficient differs from the stress-free according to the quadratic form given in Equation (38). The theoretical backscatter coefficients for iron subjected to a uniaxial loading condition (using the second- and third-order single-crystal constants shown in Table 2) were found to be $K_0 = 582.1$ GPa^2, $K_1 = 159.1$ GPa, and $K_2 = 27.86$. Thus, the scattered response for iron was expected to be nearly linear over the loading range used here, and was predicted to decrease with applied compressive load ($T < 0$).

The measurements were made using an x-y axis motorized stage that was mounted to the loading press. The configuration of the scanning process is shown in Figure 27. The sample was loaded at a constant loading rate of 178 kN/min to a maximum load of 1780 kN. At increments of 222.4 kN, the load was held constant. During the load hold, the transducer was scanned at a constant speed over the surface of the loaded sample while waveforms were collected. The scanning was performed with a step size of 3 mm to ensure the independence of individual measurements. The spatial variance of the scattered waveforms was calculated using a collection of 1,000 waveforms. This number results in a suitable signal-to-noise ratio. Eight loading steps were performed in total, such that the block was loaded in uniaxial compression over a range from 0 to 250 MPa.

This process was repeated over a set of three loading trials performed on separate days to observe the experimental repeatability. Each variance response during a given trial was fit using Equation (9) to extract the peak of the response as a function of stress. The peak responses at each loading step for the three trials are shown in Figure 29. The experimental results show a decreasing trend with increasing compressive stress, as predicted from the theory. Figure 29 also shows the corresponding theoretical curve from Equation (9), using the theoretical coefficients based on pure iron. A comparison of the theoretical backscatter coefficients of iron with the experimental backscatter coefficients from this sample of steel is given in Table 3. The experimentally extracted K_1 coefficient is about twice the predicted value determined using the theoretical constants for iron single crystals. Additional research is needed to fully understand these differences.

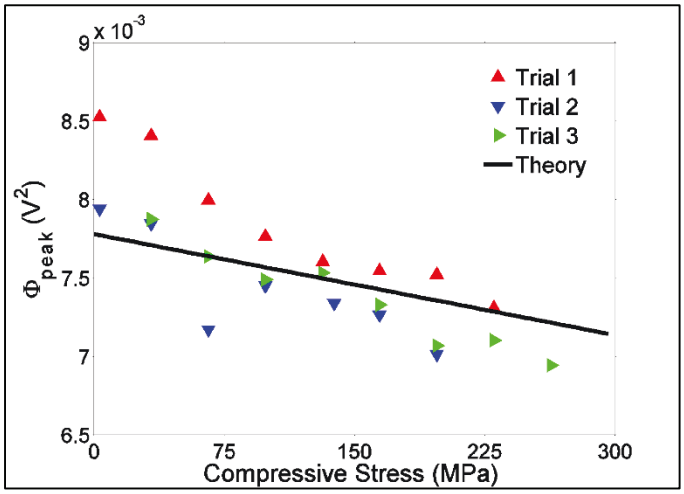

Figure 29. Change in Φ_{peak} With Increasing Compression Load for Three Loading Trials at Different Locations

The theoretical line is based on single-crystal constants for iron (Kube et al., 2012).

Table 3. Comparison of Theoretical Backscatter Coefficients of Iron and Experimentally Determined Coefficients for the Sample of Steel

Material	$K_0(GPa^2)$	$K_1(GPa)$
Pure iron (theory)	582.1	159.1
1018 steel (experiment)	602.1 ± 26.0	332.6 ± 50.8

4.2.3 Single-point Laboratory Measurements

The inconclusive backscatter results observed from using the ultrasonic scanning tank and the tensile fixture led to attempts to measure backscatter with stationary or single-point devices. Many of these devices were designed and built. One of the early designs is shown in Figure 30.

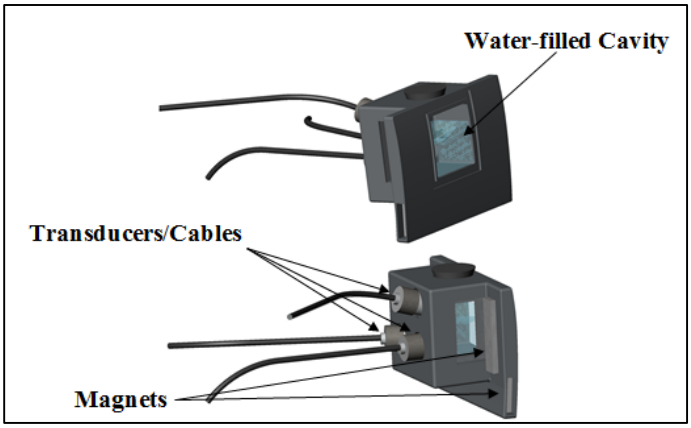

Figure 30. Initial Single-Point Diffuse Ultrasonic Backscatter (DUB) Measurement Device Designed to Perform Backscatter Testing

The device consists of a water-filled cavity, which can be attached magnetically or clamped to a testing block or rail sample. The water was needed to provide coupling for the transducers embedded into the back of the attachment. The design allows for the insertion of a normal-incidence transducer, along with two 18° angled transducers for longitudinal-to-shear wave scattering measurements. The distance from the transducer face to the surface of the material defines the depth of ultrasonic penetration into the material. It is governed by the focal depth in the material, often called the material path (*mp*), which can be defined as:

$$mp = \frac{c_w}{c_m}(F - wp) \quad , \tag{43}$$

where *F* is the focal length, *wp*, is the water path, and $\frac{c_w}{c_m}$ is the ratio of wave speeds in the water and test sample. The transducers (*Panametrics V-327SU)* used in the attachment had a center frequency of 10 MHz and contained a geometrical focal length of 2 in. The attachment was designed such that the water path of the shear transducers produced an equal material path (penetrating depth of the ultrasound). The equal material paths ensure that the ultrasound insonifies a similar number of grains through the depth of the material. This device and others that were designed were used for a large number of experiments.

Mechanical Loading Experiments on Steel and Aluminum Blocks

The ultrasonic attachments were used in conjunction with a 454,000-lb. compression loading ram (Southwark-Emery model #64305), which generated uniaxial stresses in sample blocks of steel and aluminum. The sample blocks were milled smooth so that possible surface effects were eliminated. The cross-section dimensions of the steel and aluminum blocks were 3" x 5" and 3.5" x 5.5", respectively. The loading ram compressing a steel block is shown in Figure 31.

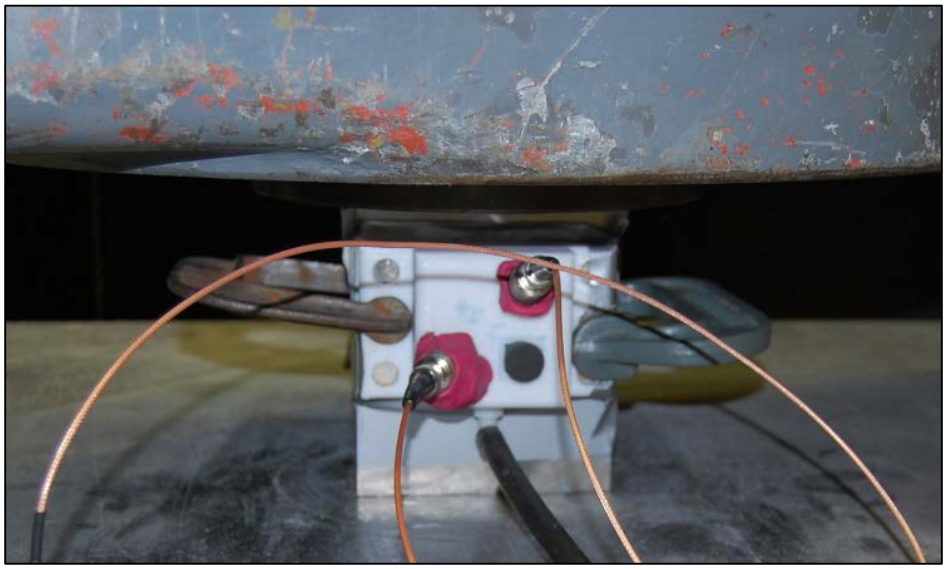

Figure 31. Loading Ram Compressing the Steel Block
The water-filled attachment is clamped to the block and houses the two shear transducers.

The blocks were loaded linearly at 80,000 lb per minute until the maximum load of 454,000 lb was reached. During the loading, ultrasonic waveforms were generated from the oblique- and normal-incidence transducers. The waveforms were collected through the use of a digitizer in the previously described computer system. The digitizer (*Mistras AD-81G-PCI*) sampled the waveforms at 500 MHz and provided 8-bit vertical resolution. Ninety waveforms were collected at equal time intervals during the loading cycles. After testing, the waveforms were post-processed using *Matlab*, and the single-point autocorrelation quantity was calculated (see Equation 41) and plotted against the corresponding stress in the block. Results for steel and aluminum are shown in Figure 32 and Figure 33. The red (Ξ_{2323}^{2323}) and green (Ξ_{1313}^{1313}) data points are from the 18º angled or shear mode transducers. The black (Ξ_{3333}^{3333}) data are from the normal incidence, longitudinal mode transducers.

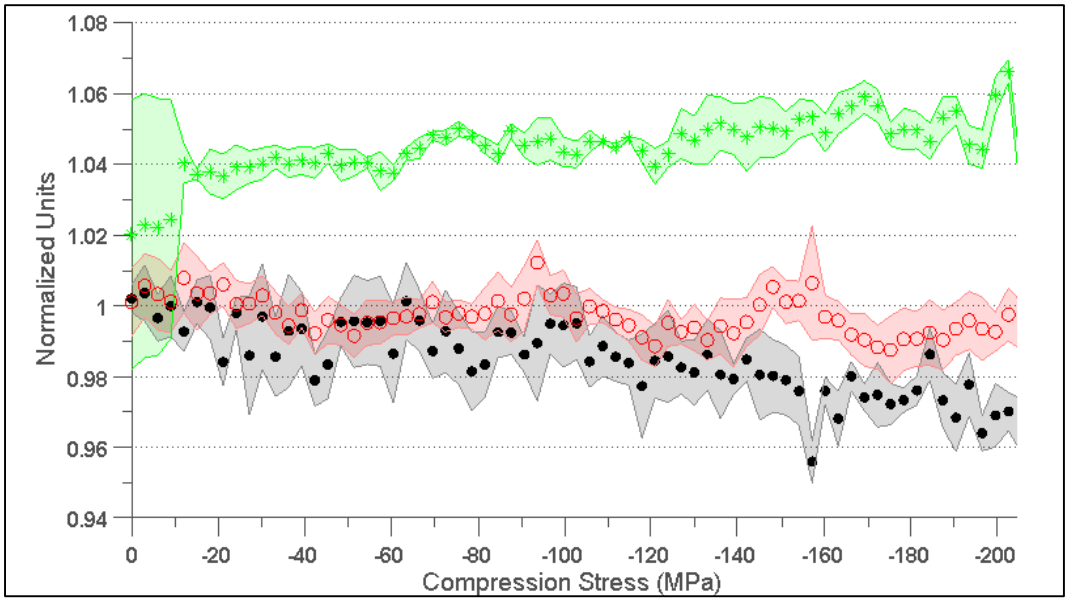

Figure 32. Normalized Backscatter Results for Uniaxial Compression of Steel

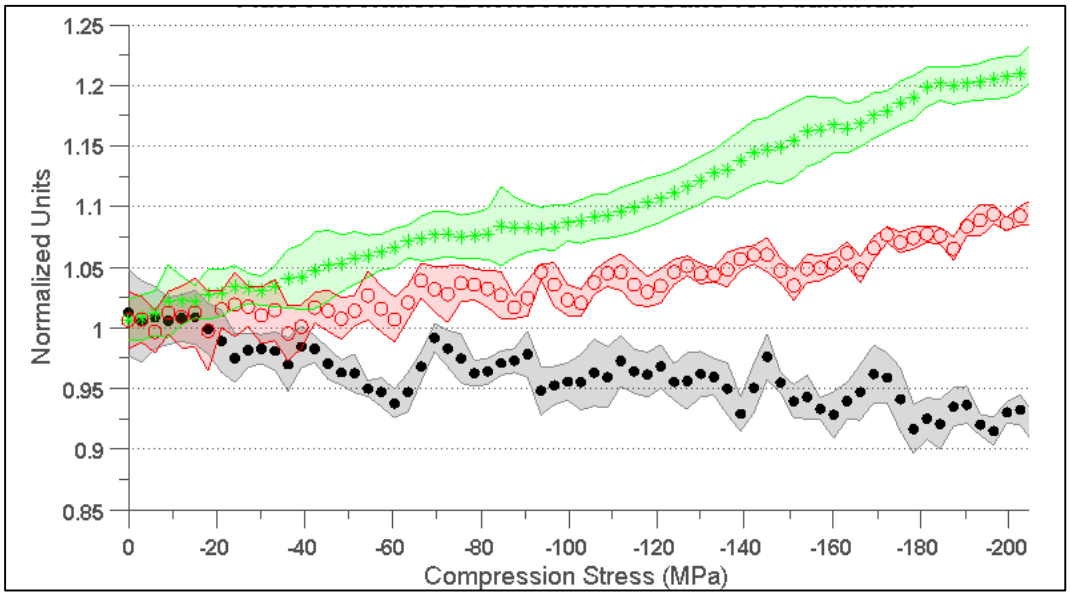

Figure 33. Normalized Backscatter Results for Uniaxial Compression of Aluminum

The data points were normalized by the zero stress value (*y*-intercept has a value of 1) to illustrate the results better, and for comparison with the theory. The normalized data were averaged over a collection of six loading trials. The six loading trials consisted of performing four trials in a given day followed by two trials the next day. After the first day, the water was drained from the device, which was reattached at a different location on the test block. The standard deviation for all six trials is represented by the colored shaded regions over the data sets of the same color. The small standard deviations indicate that the procedure is repeatable and is independent of the two attachment locations.

The corresponding theoretical normalized covariance curves for the different transducers, from the theory described in Section 3 (Turner and Ghoshal, 2010), are shown in Figure 34 and Figure 35.

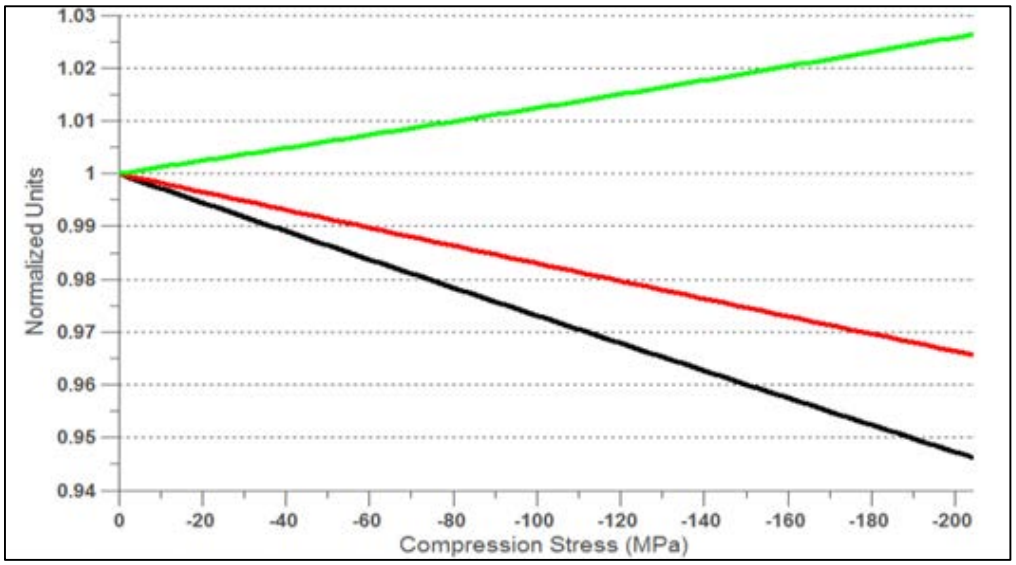

Figure 34. Theoretical Backscatter vs. Uniaxial Stress Curves for Iron
The black curve is the 3333, green is the 1313, and red is the 2323.

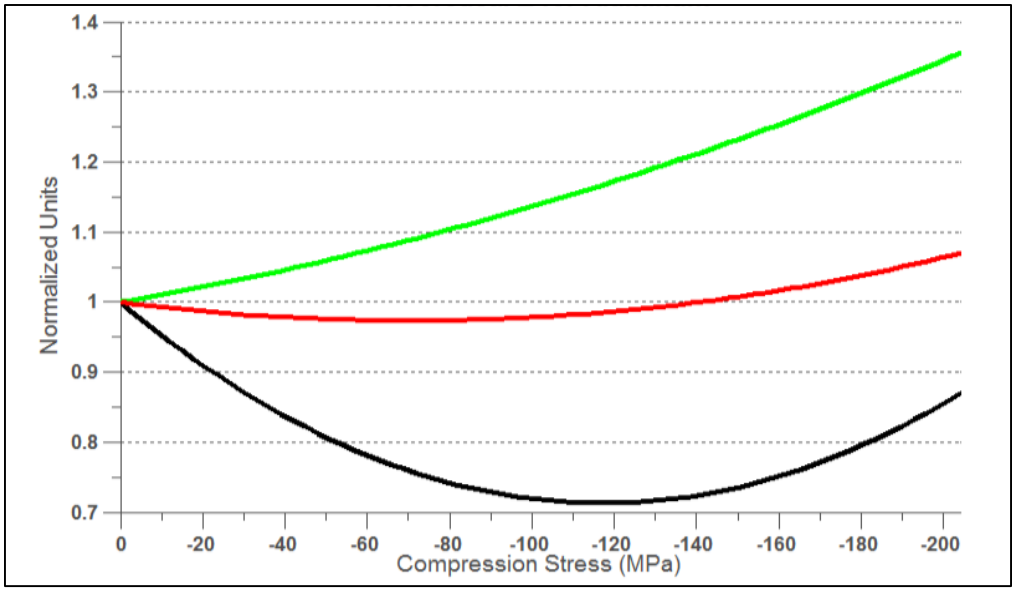

Figure 35. Theoretical Backscatter vs. Uniaxial Stress Curves for Aluminum
The black curve is the 3333, green is the 1313, and red is the 2323.

It is evident that the experimental data points follow similar trends to the theoretical curves. In both steel and aluminum, the largest change over the stress range was given by the shear (Ξ_{1313}^{1313}) transducer. The percent changes for this transducer were 21% for aluminum and 5% for steel over the loading range used. Figure 36 shows the results of backscatter measurements for six load/unload cycles. The measurements are repeatable within a 9% uncertainty band.

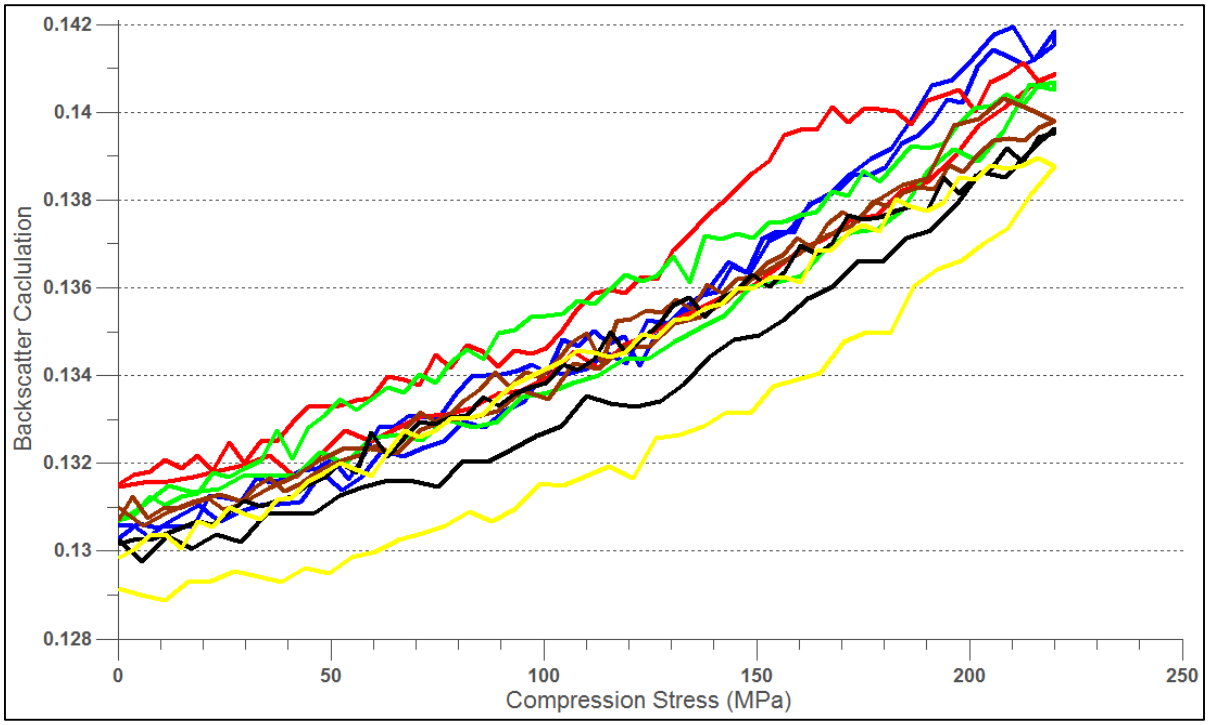

Figure 36. Repeatability Results for Six Sets of Backscatter Measurements

Comparison of Measurement Resolution Between Backscatter and Wavespeed

A comparison between the measurement resolution of backscatter and wavespeed can be made by observing the slopes of the datasets in Figure 32 and Figure 33. Table 4 shows the calculated backscatter slopes.

Table 4. Slopes of the Backscatter Data Shown in Figure 32 and Figure 33

Material	Ξ_{1313}^{1313}/MPa	Ξ_{2323}^{2323}/MPa	Ξ_{3333}^{3333}/MPa
Aluminum	$1.02x10^{-3}$	$4.89x10^{-4}$	$3.66x10^{-4}$
Steel	$2.43x10^{-4}$	$4.88x10^{-5}$	$1.46x10^{-4}$

Values are given as the measurable change per unit stress and the units are megapascal (MPa).

The slopes give an indication of the measurable change in backscatter per unit MPa stress change. Previous results (Egle and Bray, 1976) showed that the slope of measured wavespeed data was 0.57 $\frac{nsec}{MPa}$. To resolve a change in travel time on the order of nanoseconds reliably, a digitizer is needed with a sampling rate in excess of 1 GHz (10^9 $\frac{\text{points}}{\text{second}}$ of time resolution). By comparison, the changes in the diffuse ultrasonic backscatter were able to be resolved using an 8-bit (2^8 or 256 resolvable lines of amplitude) digitizer. The two methods are inherently different, in that backscatter depends on signal amplitudes, while wavespeed is strictly a temporal measurement. Manufacturers of digital signal processing (DSP) equipment currently produce digitizers that are commonly sold with 10- to 16-bit resolutions at sampling frequencies of 200 to 500 MHz. Most DSP manufacturers do not offer digitizers with sampling rates greater than 1 GHz. Those that do demand purchase costs greatly exceeding cards suitable for backscatter

GHz, and those that do demand purchase costs greatly exceeding cards suitable for backscatter measurements. Thus, an ultrasonic backscatter approach is possibly more economical as well for achieving a given measurement resolution.

Mechanical Loading Experiments on a Rail Section

The mechanical loading experiments on the blocks of steel and aluminum gave encouraging results. The experiments proved that backscatter is influenced by mechanically induced uniaxial stresses. The next step in the progression of the research was to load spans of rail section mechanically. Prior to these tests, a new ultrasonic system was purchased to allow dual-channel insonification during loading trials. The system consisted of a two-channel pulser/receiver (*JSR DPR-500*) and a PXI (*National Instruments*) based computer system (*PXI-1031 DC*) equipped with two dual-channel digitizer cards (*PXI-5124*). The digitizers have 10-bit vertical resolution with a maximum sampling rate of 200 MHz per channel. The pulser/receiver and computer system are shown in Figure 37.

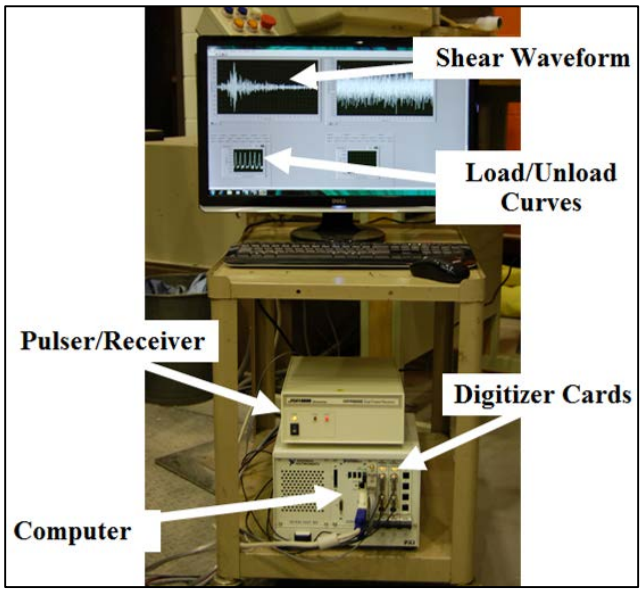

Figure 37. Two-Channel Pulser/Receiver Sitting atop the *National Instruments* Computer System

The system also eliminated the need for postprocessing through *Matlab* in order to obtain results. Real-time backscatter results were given through the use of a *Labview* virtual instrument program. These upgrades significantly reduced testing duration and were a big step toward an efficient measurement capability for field testing on CWR. The loading experiments were performed using the same compression ram discussed above. The rail section and loading ram are shown in Figure 38.

The rail section used in the loading tests was never used in service. It was cut from a larger 7-ft section of rail (132 lb/yd) to a length of 16 in. The cutting was performed through the use of an air-cooled wire cutter, which prevented residual stresses typically formed from heat-induced deformation. The cross-sectional area was 13.29 in^2, such that the 454,000-lb. compression ram generated uniaxial stresses up to 232 MPa.

Figure 38. Loading Ram Compressing the Rail Section While Two Shear Transducers Are Used to Monitor the Backscatter Signals

Ultrasound was generated using two 10-MHz focused immersion transducers (*Panametrics V-327SU*) and attached to the rail sample as shown in Figure 38. In these tests only the shear mode waveforms were acquired during loading. The loading rate was set at a constant 120,000 lbs/min until the maximum load of 454,000 lbs was reached. After loading, the compression ram relaxed back to a stress-free state. Figure 39 and Figure 40 show backscatter results over a number of loading and unloading cycles.

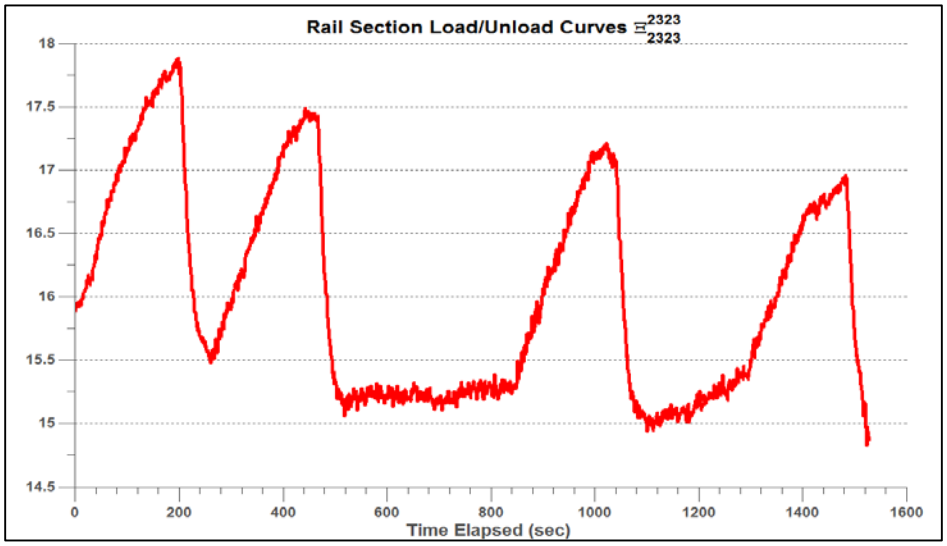

Figure 39. Plot Showing Load/Unload Curves for the (2323) Shear Mode Backscatter

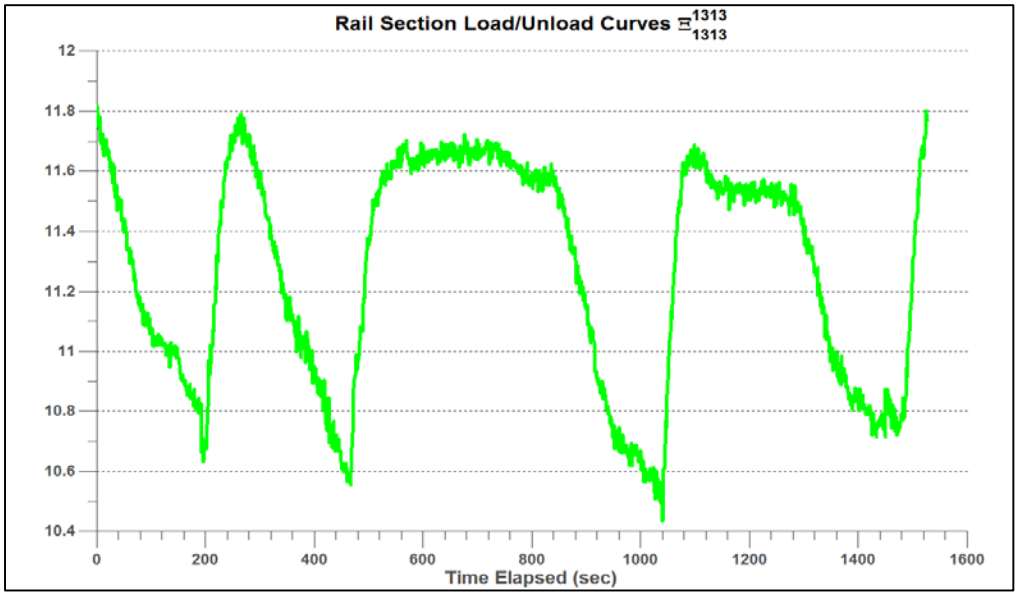

Figure 40. Plot Showing Load/Unload Curves for the (1313) Shear Mode Backscatter

The results were simultaneously obtained during the loading cycles for the two shear modes (Ξ_{2323}^{2323}in red and Ξ_{1313}^{1313} in green). In Figure 39 and Figure 40, the first load occurred during the first 190 seconds, followed by a quicker unload of 50 seconds. The results show the opposite behavior between the two shear modes during the loading and unloading cycles, as predicted by the theory. The sample rested in a stress-free state from 500 to 875 seconds. The resting period demonstrates an undeviating baseline during a stress-free state after loading cycles have been performed. The two loading cycles after the resting period displayed similar responses to the first two. For these tests, the Ξ_{2323}^{2323} shear mode gave the largest change over the stress range (0 to 232 MPa). The average percent change for this mode was 12.9%. Figure 41 and Figure 42 show results obtained from a different attachment location on the same rail section.

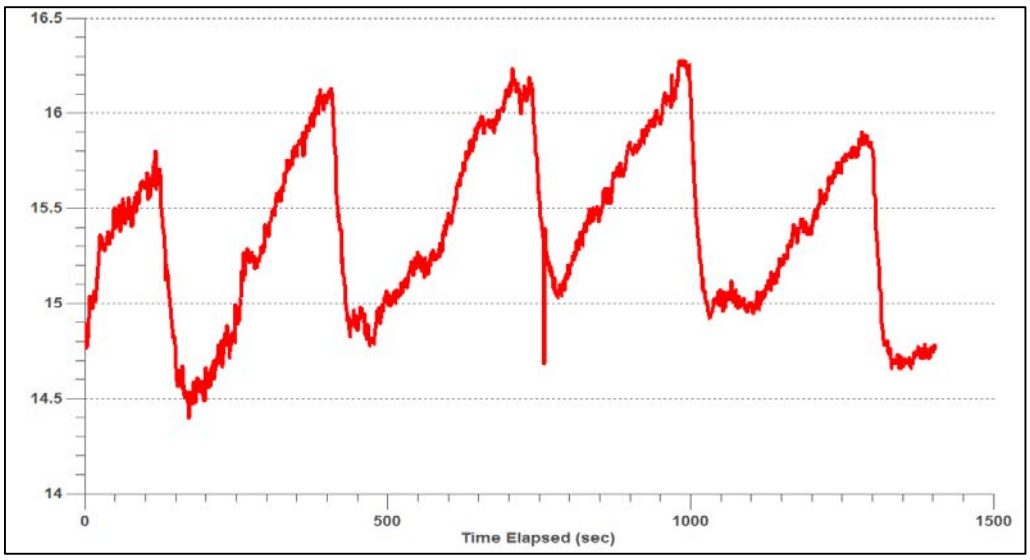

Figure 41. Plot Showing Load/Unload Curves for the (2323) Shear Mode Backscatter from Measurements at a Location Different from the Location in Figure 39 and Figure 40

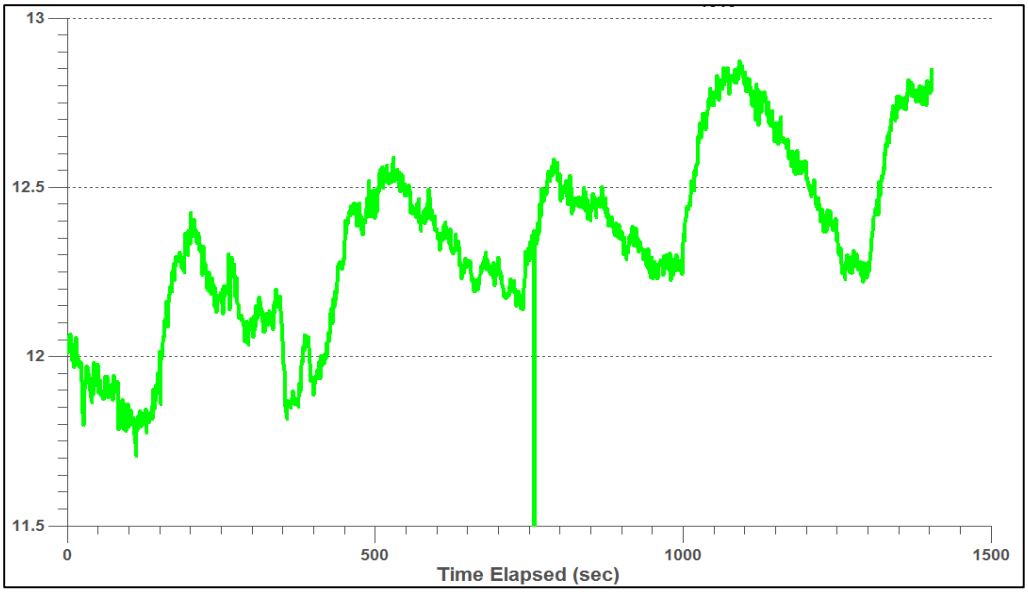

Figure 42. Plot Showing Load/Unload Curves for the (1313) Shear Mode Backscatter from Measurements at a Location Different from the Location in Figure 39 and Figure 40

These results utilized the same pulser/receiver settings and the same window region for the backscatter calculation. Similar trends were observed in these results (between Figures 39 and 40 and Figures 41 and 42) when comparing the shear modes at the different locations. The second location gave slightly noisier results along with a noticeable upward trend over the five loading and unloading cycles for Ξ_{2323}^{2323}.

The noise and the upward trend were not believed to have been caused by the compression ram or signal acquisition/processing. The water-filled attachment appeared to be sensitive to any slight form of agitation. Minute leaks or bumping the transducer cables caused noticeable influences on the backscatter calculation. The sudden decrease seen in Figure 42 was caused by agitating the cable/transducer. In many trials, fresh water placed into the attachment caused the baseline stress-free backscatter result to increase or decrease linearly. The cause of these trending baselines could not be determined but was believed to be either a temperature effect of the water or the formation of air bubbles on the surface of the transducer or rail.

These results show that backscatter measurements on a section of rail are able to track induced mechanical stresses. The measurements also demonstrated the ability to apply these techniques to samples that had slight corrosion or oxidation, without the need for surface treatments.

4.3 Field Tests on the Union Pacific Railroad

A series of field tests were performed on a heavy-haul line of the Union Pacific Railroad (UP) in order to explore the feasibility of the diffuse ultrasonic backscatter method for in-service rail. The rail site was on the South Morrill subdivision near milepost 47 (Figure 43). At this site, UP has nine stress modules installed. Each stress module contains strain gauges and thermocouples in order to measure both stress and temperature in real time. The stress modules allow for quantitative comparisons between ultrasonic backscatter measurements and thermal stress/temperature. The single-point rail attachment (Figure 44) was used to collect scattered ultrasonic waveforms at the various locations near the stress modules. Ultrasonic transducers were attached to the web of the rail and remained in place while the track was in service (Figure 45).

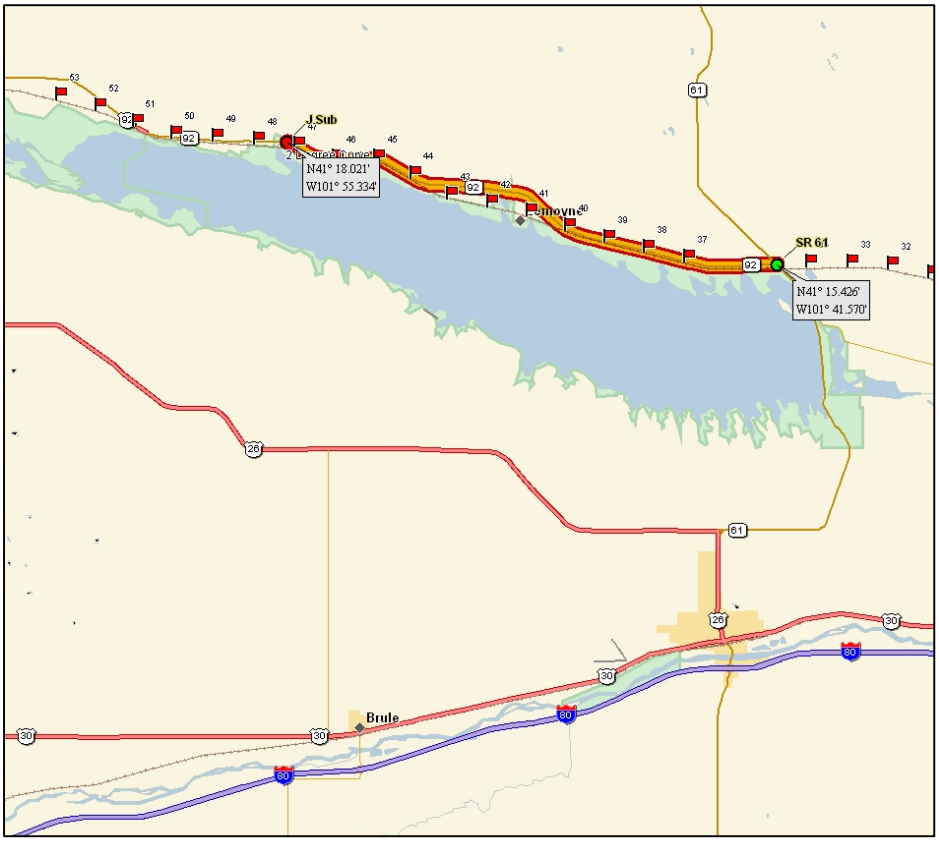

Figure 43. Map of the UP Stress Module Test Site on the South Morrill Subdivison, Near MP 47

The site is in western Nebraska on the north side of Lake McConaughy.

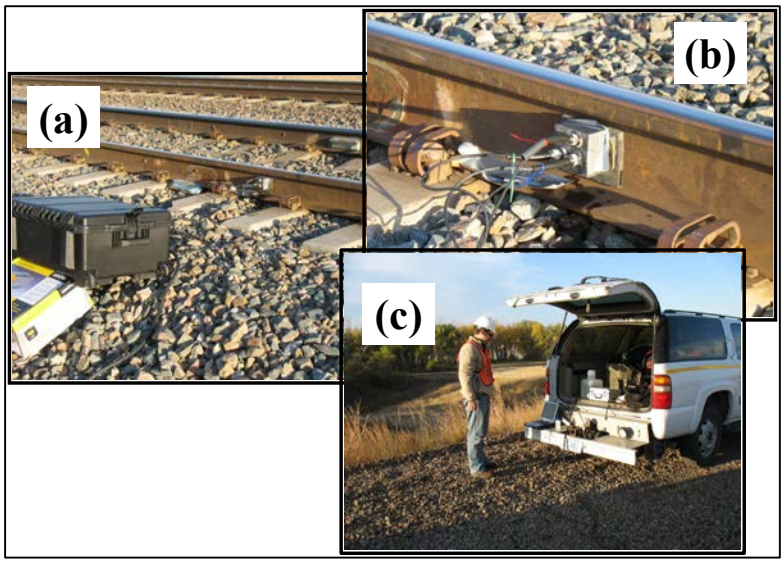

Figure 44. Portable Ultrasonic System Operated from a Rail Vehicle Next to the Testing Locations

Figure 45. Ultrasonic Transducers Attached to the Web of the Rail, Remaining in Place While the UP Track Was in Service

This result was the first set of field tests performed with this portable system. Backscatter, stress, and temperature measurements were acquired throughout the day, starting near dawn when the rail temperature was well below the RNT. The autocorrelation procedure described in Section 4.1.2 was used to quantify the backscatter. Figure 46 shows the trends of backscatter vs. stress and backscatter vs. temperature. The correlation between these quantities is clear over the loading and temperature ranges. Figure 46 also shows the effect that a moving train has during the measurement. The device attaches to the web of the rail such that measurements are not disrupted by trains. The signal become sporadic during the train motion but stabilizes soon after the train passes.

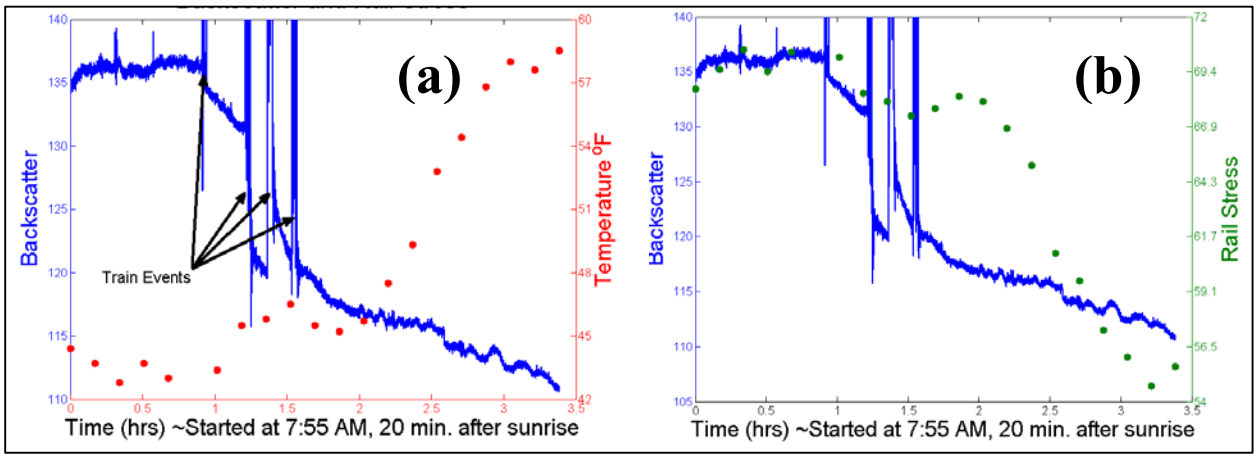

Figure 46. Example Result from UP Measurements
The ultrasonic backscatter clearly tracks the stress due to the thermal expansion. Train arrivals are shown to disrupt the measurements temporarily, but the trends are resumed after the trains pass.

4.4 Development of Field Test Site on Omaha, Lincoln and Beatrice Railway

To allow a greater number of field measurements to be made, a field test site was developed in collaboration with the Omaha, Lincoln and Beatrice (OL&B) Railway and the Burlington Northern Santa Fe Railway (BNSF). A spur between the BNSF main line and OL&B was chosen for installation of four rail stress modules. Maps showing the approximate site location within the city of Lincoln, NE, are shown in Figure 47. The approximate locations of stress modules 1-3 are shown in Figure 48.

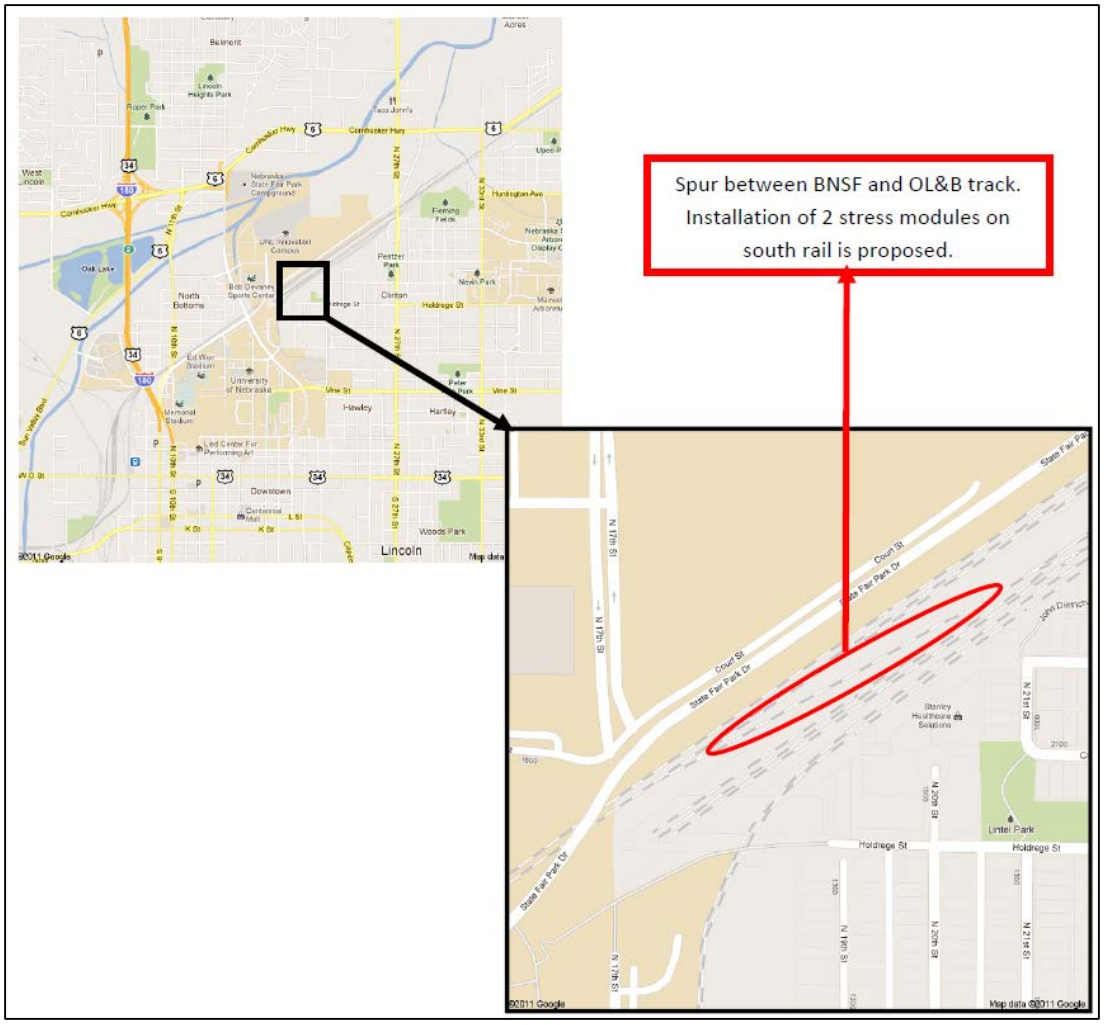

Figure 47. Location of Spur Between the BNSF Main Line and the OL&B Railway Where Four Rail Stress Modules Were Installed

On October 28, 2011, the four stress modules were installed by Instrumentation Services, Inc. A readout box was provided by BNSF for use in this project to monitor the local strain, stress, temperature, and RNT through a wireless interface with a computer. The readings were taken at prescribed intervals, with the information recorded with a time marker. The installation procedure involved polishing the rail on both sides at the approximate location of the neutral axis for bending. Strain gauge rosettes were welded on to the polished surfaces and covered with a waterproof cover. In addition, a thermocouple was attached so that temperature measurements could be made as well. The locations were marked with a paint marker to identify the specific

gauge. The four installation sites are shown in Figure 49. The silver protective covering can be observed with the sets of wires for the measurements shown. Each set of wires was fitted with a connection that could be attached to the readout box.

Figure 48. Approximate Locations of Stress Modules 1-3
The site of module 4 is outside this image to the upper right.

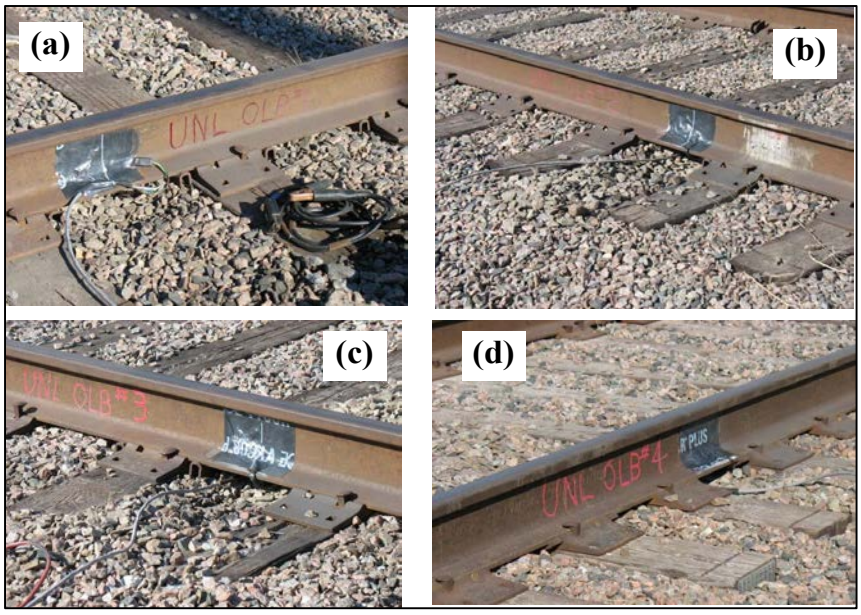

Figure 49. Photographs of the Four Stress Module Installation Sites

The stress modules were calibrated by Rail Sciences, Inc. on January 11, 2012, using the rail uplift method, which involved unclipping ~50 ft. of rail on each side of the stress module (Figure 50, a and b). A calibrated lifting device, was then used to raise the rail while the load required for lifting as well as the rail deflection were monitored (Figure 50, c and d). The information was used to determine the current axial load in the rail. The basic idea behind this method was analogous with the lifting of a string or wire that was under tension. The more force needed to lift the rail, the higher the axial load. Obviously, this technique can be applied only when the rail is under tension. The RNT at each site was noted on the rail with paint marker at each location. RNT was quite low by most rail standards, in the range of 77 °F.

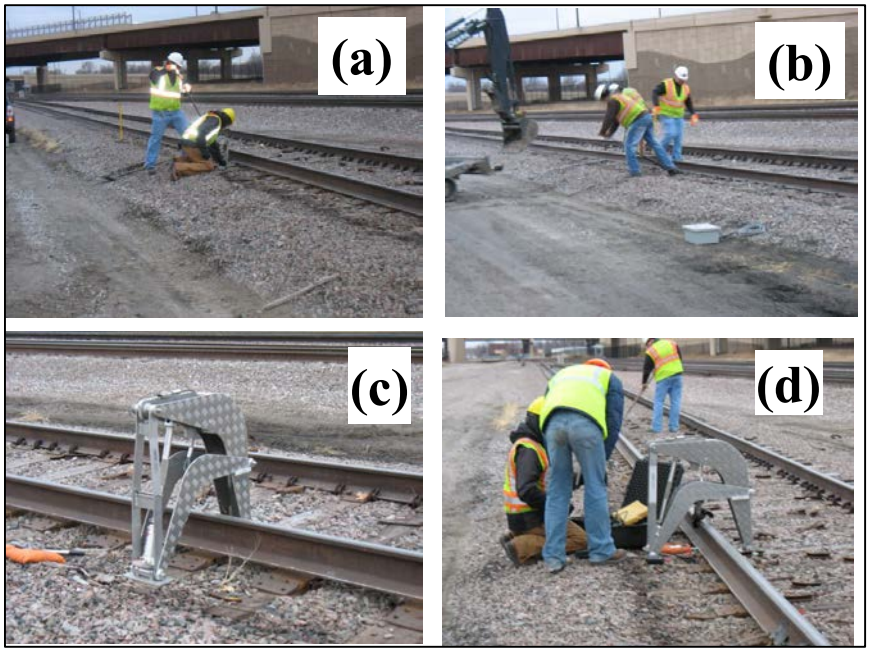

Figure 50. Stress Module Calibration on January 11, 2012
Modules were calibrated using the rail uplift method: the rail is first unclipped [(a) and (b)], then lifted with an uplift device [(c) and (d)], and the load and deflection are recorded.

Both single point and scanning backscatter measurements were performed at this site and compared with the temperature and force data from the installed strain gauges. The single point measurements were made with the same equipment used for the testing performed during the UP field tests (Figure 51). An autocorrelation algorithm was used to quantify the backscatter for the single point measurements. An example dataset for backscatter vs. force is shown in Figure 52.

Figure 51. Single Point Measurement at the OL&B Railway

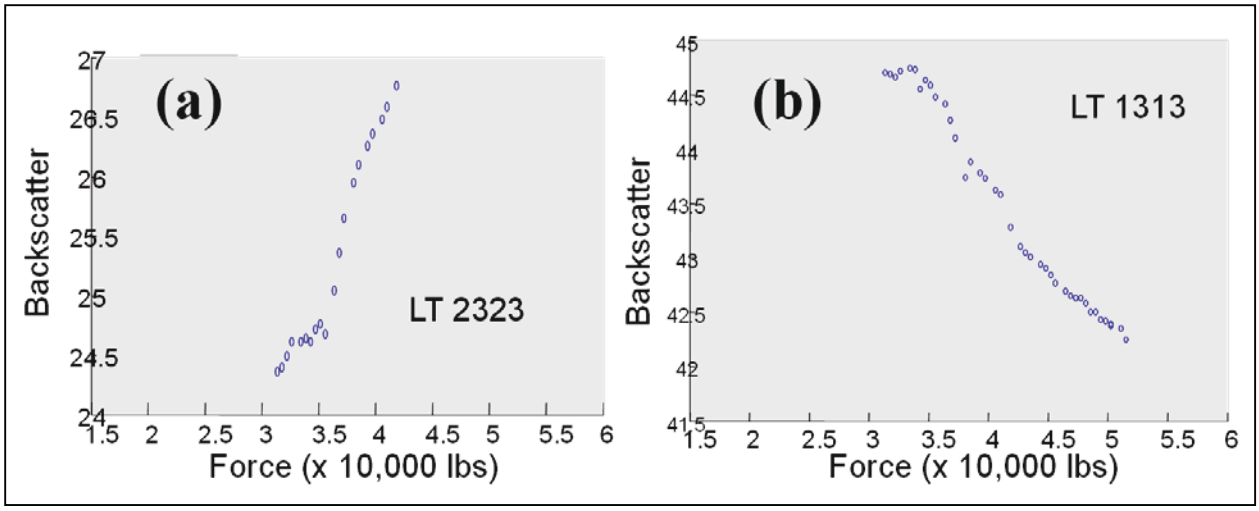

Figure 52. Single Point Diffuse Ultrasonic Backscatter Measurements at the OL&B Test Site

These results show the dependence of mode-converted shear backscattered signals to applied tensile forces. The LT2323 measurements contain scattering and polarization directions out of plane with the stress direction. Conversely, the LT1313 measurements contain a scattering component and polarization component that lie in the uniaxial stress plane. Similar to the results shown in Figure 41 and Figure 42, the slopes are approximately equal in magnitude but have opposite signs. The magnitude of the scattering in these cases should be equal at zero stress. Thus, performing a measurement when these two quantities are equal may indicate that the rail is nearly stress-free.

A scanning box enclosure (Figure 53, a) was designed to allow SSR measurements to be performed in the field. Scanning measurements allow the application of the theoretical SSR model presented in Section 2 and the stress-dependent model described in Section 3 to be applied. A triad of transducers was mounted within the enclosure on a lead screw to allow the transducers to be positioned at different locations along the web of the rail. The enclosure box was then attached magnetically to the rail and sealed (Figure 53, b).

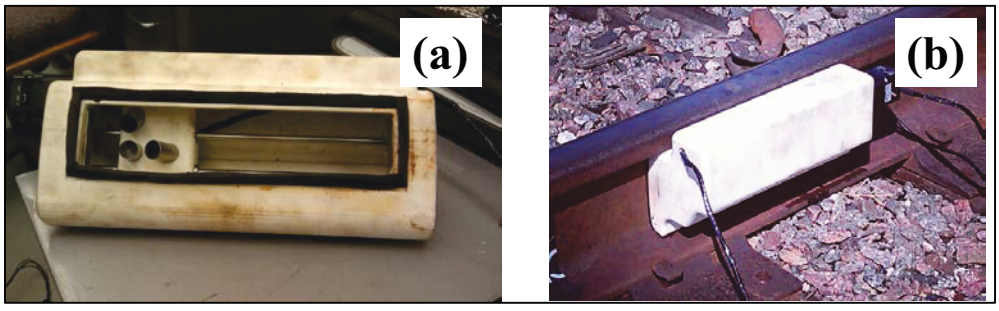

Figure 53. Scanning Box Designed for Rail Measurements

The scanning rail attachment box was used to collect waveforms and analyze the spatial variance of the waveforms. The strain data were converted into force for comparison with the backscatter measurements. Figure 54 shows the results from LT1313 scattering. The different colored backscattered traces were from scattering measurements performed at different levels of

compression force present in the rail. The noise in the signal is due to the grain scattering process. The peak amplitudes show a weak decreasing correlation with the increasing amount of force.

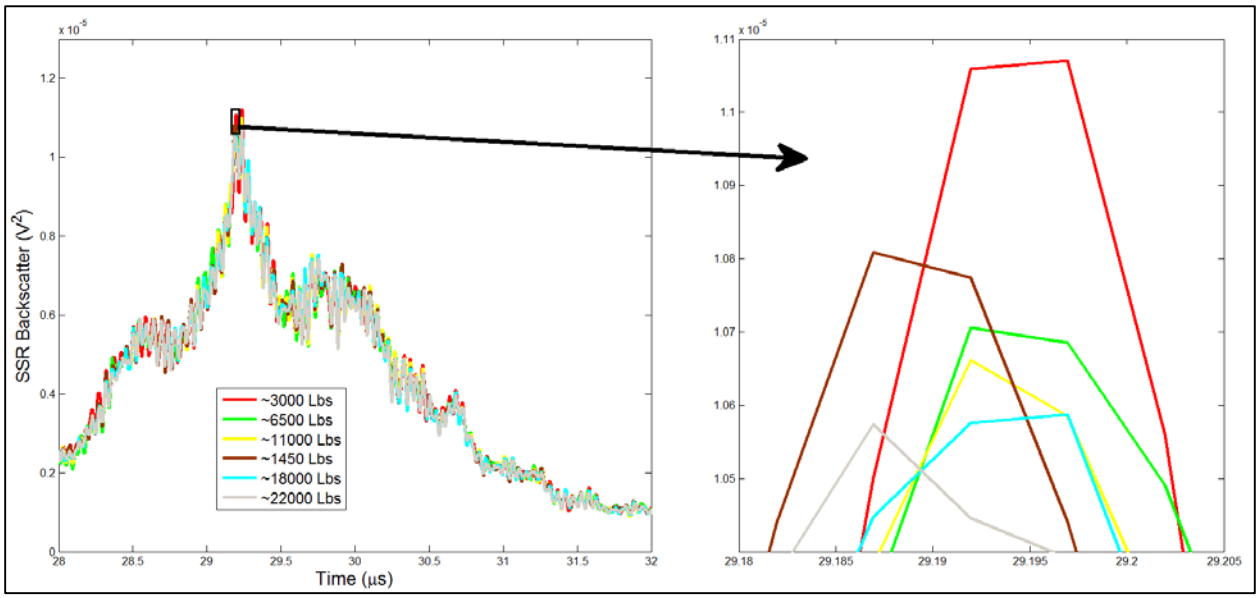

Figure 54. Backscatter SSR Results for the Shear Scattering Mode LT1313, Made Using the Scanning Box Shown in Figure 53

The level of noise present in SSR measurements makes it difficult to resolve the scattering peaks clearly and the corresponding trends with stress. The amplitude changes with stress also differ, depending on which point in time is considered. Although many measurements were made using these different approaches, signal drift made it difficult to obtain results that allowed an estimate of the stress state to be made.

4.5 Summary

In this section, the experimental efforts associated with the diffuse ultrasonic backscatter measurements were described. Two primary measurement approaches were used. One involved direct scanning of the transducers along the rail web, enabling the determination of spatial variance curves for comparison with the theoretical expectations discussed in Section 2 and Section 3. The other used an alternative signal processing methodology in the form of the autocorrelation function applied to a windowed portion of the backscattered signal. Both approaches were applied to measurements in the laboratory and in the field, using several different versions of the measurement device that were designed and manufactured.

In addition, a field laboratory test site was developed for this project near the UNL campus. This test site included four working stress modules at locations along a spur near the BNSF main line. The site and the associated stress module data provided an excellent base that could be used for comparison with future stress monitoring equipment. The controlled environment and low-traffic conditions were ideal for the development and testing of new measurement approaches.

All experimental results presented in this section were very encouraging. Both signal processing approaches showed clear trends in the measured backscattered signals with respect to load.

Laboratory measurements were clearly more repeatable and were much less susceptible to variations during testing over the course of several days. The field measurements showed that diffuse ultrasonic measurements could be made on in-service rail, and the clear trends observed over the course of each test day were in line with the measured rail loads determined from stress modules. Unfortunately, for all measurement configurations explored, it was not possible to achieve signal levels that were sufficiently repeatable over the course of time to allow stress estimates to be made reliably. Several attempts were made to reduce the signal drift and correct it, but a suitable method was not achieved.

5. Conclusion

In this project, the application of diffuse ultrasonic measurements was examined for possible application to measurement of longitudinal rail stress. Although a final measurement device has not yet resulted from this research, several successful outcomes have been achieved:

- A quantitative model to describe the diffuse ultrasonic backscatter from a polycrystalline material was developed, including a complete measurement system. The model was derived for an arbitrary transducer configuration (pulse-echo or pitch-catch) in a generalized way. It was shown to allow successful determination of the material grain size from spatial variance measurements.
- The theoretical basis relating ultrasonic scattering from a polycrystalline material to the applied stress was developed for the first time. Although wave speed has been recognized as being dependent on stress, the scattering effects had not been previously explored. This work will likely have application to other problems, such as residual stress determination.
- Clear trends in the diffuse ultrasonic scattering were observed with respect to sample stress in a wide range of tests, covering tension and compression for both laboratory and field measurements. Conditions involving both mechanical stresses and thermally generated stresses led to significant changes in the scattering with stress. This connection between scattering and stress were previously unknown, and comparisons with the related theory were encouraging.
- The capability of performing diffuse ultrasonic backscatter measurements at field test sites was demonstrated for the first time. Measurements were also made on rail still in service. This work may have other future applications associated with quantifying the local sample texture or identifying subsurface defects that may be present in the rail.
- A measurement test site that included four stress modules was developed to allow a large number of measurements to be performed.

Several different attempts were made to correct for drift in the measurements that were observed over time. Although a successful correction was not found within the time frame of this project, this work will provide insight into possible alternative measurement approaches that would allow quantitative measurements of stress to be made.

6. References

1. American Association of Railroads. (2013). *Chronology of Railroading in America*. https://www.aar.org/BackgroundPapers/Chronology%20of%20RRs%20in%20America.pdf.
2. Ballabh, T.K., Paul, M., Middya, T.R., & Basu, A.N. (1992). Theoretical multiple-scattering calculation of nonlinear elastic constants of disordered solids. *Physical Review B*, *45*, 2761-2771. http://journals.aps.org/prb/abstract/10.1103/PhysRevB.45.2761.
3. Bergman, R.H., & Shahbender, R.A. (1958). Effect of statically applied stresses on the velocity of propagation of ultrasonic waves. *Journal of Applied Physics*, *29*, 1736-1738. http://aip.scitation.org/doi/abs/10.1063/1.1723035.
4. Carrier, G.F., Krook, M., & Pearson, C.E. (1983). Complex Analysis and Conformal Mapping, *Functions of a Complex Variable: Theory and Technique*, pp. 318-325 . Ithaca, NY: HOD Books. http://trove.nla.gov.au/work/21958396?q&versionId=26464715.
5. Egle, D.M, & Bray, D.E. (1976). Measurement of acoustoelastic and third-order elastic constants for rail steel. *Journal of the Acoustical Society of America*, *60*, 741-744. http://asa.scitation.org/doi/abs/10.1121/1.381146.
6. Ghoshal, G., Turner, J.A., & Weaver, R.L. (2007). Wigner distribution of a transducer beam pattern within a multiple scattering formalism for heterogeneous solids. *Journal of the Acoustical Society of America*, *122*, 2009-2021. http://www.ncbi.nlm.nih.gov/pubmed/17902838.
7. Ghoshal, G., & Turner, J.A. (2010). Diffuse ultrasonic backscatter at normal incidence through a curved interface. *Journal of the Acoustical Society of America*, *128*, 3449-3458. http://asa.scitation.org/doi/abs/10.1121/1.381146.
8. Hu, P., Kube, C.K., Koester, L.W., & Turner, J.A. (2013). Mode-converted diffuse ultrasonic backscatter. *Journal of the Acoustical Society of America*, *134*, 982-990. http://asa.scitation.org/doi/full/10.1121/1.4812769.
9. Kim, N., Hong, M. (2009). Measurement of axial stress using mode-converted ultrasound. *NDT & E International*, *42*, 164-169. http://asa.scitation.org/doi/full/10.1121/1.4812769.
10. Kube, C.M., Du, H., Ghoshal, G., Turner, J.A. (2012). Stress-dependent changes in the diffuse ultrasonic backscatter coeffcient in steel: Experimental results. *Journal of the Acoustical Society of America*, *132*, EL43-EL48. http://asa.scitation.org/doi/full/10.1121/1.4812769.
11. Larose, E., Hall, S. (2009). Monitoring stress related velocity variation in concrete with a 2 x 10^{-5} relative resolution using diffuse ultrasound. *Journal of the Acoustical Society of America*, *125*, 1853-1856. http://asa.scitation.org/doi/full/10.1121/1.3079771.
12. Lobkis, O.I., Rokhlin, S.I. (2010). Characterization of polycrystals with elongated duplex microstructure by inversion of ultrasonic backscattering data. *Applied Physics Letters*, *96*, 161905. http://aip.scitation.org/doi/pdf/10.1063/1.3416910.
13. Margetan, F.J., Gray, T.A., Thompson, R.B. (1991). A Technique for Quantitatively Measuring Microstructurally Induced Ultrasonic Noise. *Review of Progress in Quantitative Nondestructive Evaluation*, *10*, 1721-1728. http://lib.dr.iastate.edu/qnde/1991/allcontent/76/.

14. Payan, C., Garnier, V., Moysan, J., Johnson, P.A. (2009). Determination of third order elastic constants in a complex solid applying coda wave interferometry. *Applied Physics Letters*, *94*, 011904. http://aip.scitation.org/doi/full/10.1063/1.3064129.

15. Powell, B.E., Skove, M.J. (1984). Linear and volume compressibilities and isothermal third-order elastic constants. *Journal of Applied Physics*, *56*, 1548-1549. http://aip.scitation.org/doi/abs/10.1063/1.334114.

16. Santos, A., Bray, D.E. (2000). Ultrasonic stress measurement using PC based and commercial flaw detectors. *Review of Scientific Instruments*, *71*, 3464-3469. http://aip.scitation.org/doi/abs/10.1063/1.1287339.

17. Sinha, B.K., Tanski, W.J. (1985). Influence of biasing stresses on the propagation of surface waves. *Journal of Applied Physics*, *57*, 767-776. http://aip.scitation.org/doi/abs/10.1063/1.334725.

18. Schmerr, L.W., Song, S.J. (2007). *Ultrasonic Nondestructive Evaluation System* (pp. 95-114, 507-529). Springer, New York https://link.springer.com/book/10.1007/978-0-387-49063-2.

19. Schmerr, L.W. (2000). A Multi-Gaussian Ultrasonic Beam Model for High Performance Simulation on a Personal Computer. *Materials Evaluation*, *58*(2), 882-888.

20. Szelazek, J. (1992). Ultrasonic measurement of thermal stress in continuously welded rail with ultrasonic technique. *NDT & E International*, *25*(2), 77-85. http://www.sciencedirect.com/science/article/pii/0963869592904975.

21. Szelazek, J. (1998). "Ultrasonic measurement of thermal stresses in continuously welded rail with ultrasonic technique." European Conference on NDT'. Copenhagen.

22. Sorokin, B.P., Turchin, P.P., Glushkov, D.A. (1994). Elastic nonlinearity and propagation of volume acoustic waves under conditions of homogeneous mechanical stresses in a $La_3Ga_5SiO_{14}$ single crystal. *Physics of the Solid State*, *36(10)*, 1545-1550. http://adsabs.harvard.edu/abs/1994PhSS...36.1545S.

23. Stanke, FE, Kino, GS (1984). A unified theory for elastic wave propagation in polycrystalline materials. *Journal of the Acoustical Society of America*, 75, 665-681. http://asa.scitation.org/doi/abs/10.1121/1.390577.

24. Thompson, R.B., Lopes, E.F. (1984). The effects of focusing and refraction on Gaussian ultrasonic beams. *Journal of Nondestructive Evaluation*, *4*, 107-123. https://link.springer.com/article/10.1007/BF00566401.

25. Thompson, R.B., Margetan, F.J., Haldipur, P., Yu, L., Li, A., Panetta, P., Wasan, H. (2008). Scattering of elastic waves in simple and complex polycrystals. *Wave Motion*, 45, 655-674. http://www.sciencedirect.com/science/article/pii/S0165212507001023.

26. Turner, J.A., Ghoshal, G. (2010). Polycrystals under applied loads: Second-order grain statistics. *Applied Physics Letters*, 97, 031907. http://aip.scitation.org/doi/full/10.1063/1.3464291.

27. Weaver, R.L. (1990). Diffusivity of ultrasound in polycrystals. *Journal of the Mechanics and Physics of Solids*, *38*(1), 55-86. http://www.sciencedirect.com/science/article/pii/002250969090021U.

28. Yang, J., Hu, Y. (2004). Mechanics of electroelastic bodies under biasing fields. *Applied Mechanics Review*, *57*(3), 173-189. http://appliedmechanicsreviews.asmedigitalcollection.asme.org/article.aspx?articleid=1397983.

Abbreviations and Acronyms

A/D	analog-to-digital
BNSF	Burlington Northern Santa Fe Railway
CWR	continuously welded rail
DSP	digital signal processing
DUB	diffuse ultrasonic backscatter
kN	kilonewtons
LL	longitudinal-to-longitudinal
LT	longitudinal-to-transverse
MPa	Megapascal
MP	material path
OL&B	Omaha, Lincoln, and Beatrice Railway
PC	personal computer
POI	Plane of Incidence
RNT	rail neutral temperature
SSR	singly-scattered response
UNL	University of Nebraska-Lincoln
UP	Union Pacific Railroad